Article

Ultralow-resistance electrochemical capacitor for integrable line filtering

https://doi.org/10.1038/s41586-023-06712-2

Received: 26 April 2023

Accepted: 4 October 2023

Published online: 15 November 2023

Check for updates

Yajie Hu[1,2,6], Mingmao Wu[3,6], Fengyao Chi[1,2], Guobin Lai[3,4], Puying Li[1,2], Wenya He[1,2], Bing Lu[1,2], Chuanxin Weng[1,2], Jinguo Lin[4], Fengen Chen[1,2], Huhu Cheng[1,2], Feng Liu[4], Lan Jiang[5] & Liangti Qu[1,2]✉

Electrochemical capacitors are expected to replace conventional electrolytic capacitors in line filtering for integrated circuits and portable electronics[1–8]. However, practical implementation of electrochemical capacitors into line-filtering circuits has not yet been achieved owing to the difficulty in synergistic accomplishment of fast responses, high specific capacitance, miniaturization and circuit-compatible integration[1,4,5,9–12]. Here we propose an electric-field enhancement strategy to promote frequency characteristics and capacitance simultaneously. By downscaling the channel width with femtosecond-laser scribing, a miniaturized narrow-channel in-plane electrochemical capacitor shows drastically reduced ionic resistances within both the electrode material and the electrolyte, leading to an ultralow series resistance of 39 mΩ cm^2 at 120 Hz. As a consequence, an ultrahigh areal capacitance of up to 5.2 mF cm^{-2} is achieved with a phase angle of −80° at 120 Hz, twice as large as one of the highest reported previously[4,13,14], and little degradation is observed over 1,000,000 cycles. Scalable integration of this electrochemical capacitor into microcircuitry shows a high integration density of 80 cells cm^{-2} and on-demand customization of capacitance and voltage. In light of excellent filtering performances and circuit compatibility, this work presents an important step of line-filtering electrochemical capacitors towards practical applications in integrated circuits and flexible electronics.

Line filtering is crucial for precision power supply to integrated circuits such as central processing units (CPUs) and memory devices[15,16]. For circuit miniaturization and device portability, electrochemical capacitors can be used as an alternative to conventional electrolytic capacitors (ELCs) because of their high specific capacitance[1–8]. However, the practical application of the electrochemical capacitors in line-filtering circuits remains a huge challenge because of the difficulty in achieving fast responses, high specific capacitance, miniaturization and circuit-compatible integration simultaneously[1,4,5,9–12]. To meet fast responses, the specific capacitance has to be severely compromised as a result of the intrinsically high series resistance of electrochemical capacitors[1,4,17]. At the rectified power supply frequency of 120 Hz, the typical resistor–capacitor time constant (τ_{RC}) of general electrochemical capacitors (τ_{RC} = SR × C; where SR is the series resistance and C is the capacitance) is around 1 s, far inferior to the basic requirement of efficient line filtering (τ_{RC} < 0.23 ms, corresponding to a phase angle of φ < −80° (refs. 1,4,18)).

In this regard, series resistance reduction is the prerequisite for the realization of fast responses while retaining large specific capacitance. For line-filtering electrochemical capacitors, series resistance is mainly dominated by ionic resistance[9,19,20], including that in the electrode materials (R_m) and bulk electrolyte (R_b) (Fig. 1a). Their values can be reflected in different regions of the Nyquist diagram owing to their disparate typical response times[21] (Fig. 1b). According to the equation $\varphi = -\arctan\left(\frac{1}{\omega\tau_{RC}}\right)$, at specified frequency ω and capacitance C, the decrease of φ necessitates the reduction of R_m and R_b. So far, marked advance has been made to solely reduce R_m by loosening the pores in electrode materials[1,4,5,8,22,23]. However, there are severe limitations because of the concomitant capacitance loss as a result of the inevitable sacrifice of ionic storage sites (Extended Data Fig. 1a,b and Supplementary Note 1). To balance the frequency characteristic and capacitance, even with precise nano-treatment of electrode materials[4,13], series resistance reduction has a limit of around 100 mΩ cm^2. As a consequence, the areal capacitance (C_A) of line-filtering electrochemical capacitors remains limited (<3 mF cm^{-2}) at φ < −80°. Meanwhile, the unsatisfied miniaturization and low integration density further restrict the implementation of line-filtering electrochemical capacitors in integrated circuits until now[5,12,24,25].

Here we propose an electric-field enhancement strategy to promote ionic migration within both electrode material and electrolyte, leading to a drastic reduction of series resistance by an order of magnitude (Fig. 1c). Unlike conventional strategy that makes a trade-off

[1]Key Laboratory of Organic Optoelectronics and Molecular Engineering, Ministry of Education, Department of Chemistry, Tsinghua University, Beijing, People's Republic of China. [2]Laboratory of Flexible Electronics Technology, Tsinghua University, Beijing, People's Republic of China. [3]Key Laboratory of Eco-materials Advanced Technology, College of Materials Science and Engineering, Fuzhou University, Fuzhou, People's Republic of China. [4]The State Key Laboratory of Nonlinear Mechanics, Institute of Mechanics, Chinese Academy of Sciences, Beijing, People's Republic of China. [5]Laser Micro-/Nano-Fabrication Laboratory, School of Mechanical Engineering, Beijing Institute of Technology, Beijing, People's Republic of China. [6]These authors contributed equally: Yajie Hu, Mingmao Wu. ✉e-mail: lqu@mail.tsinghua.edu.cn

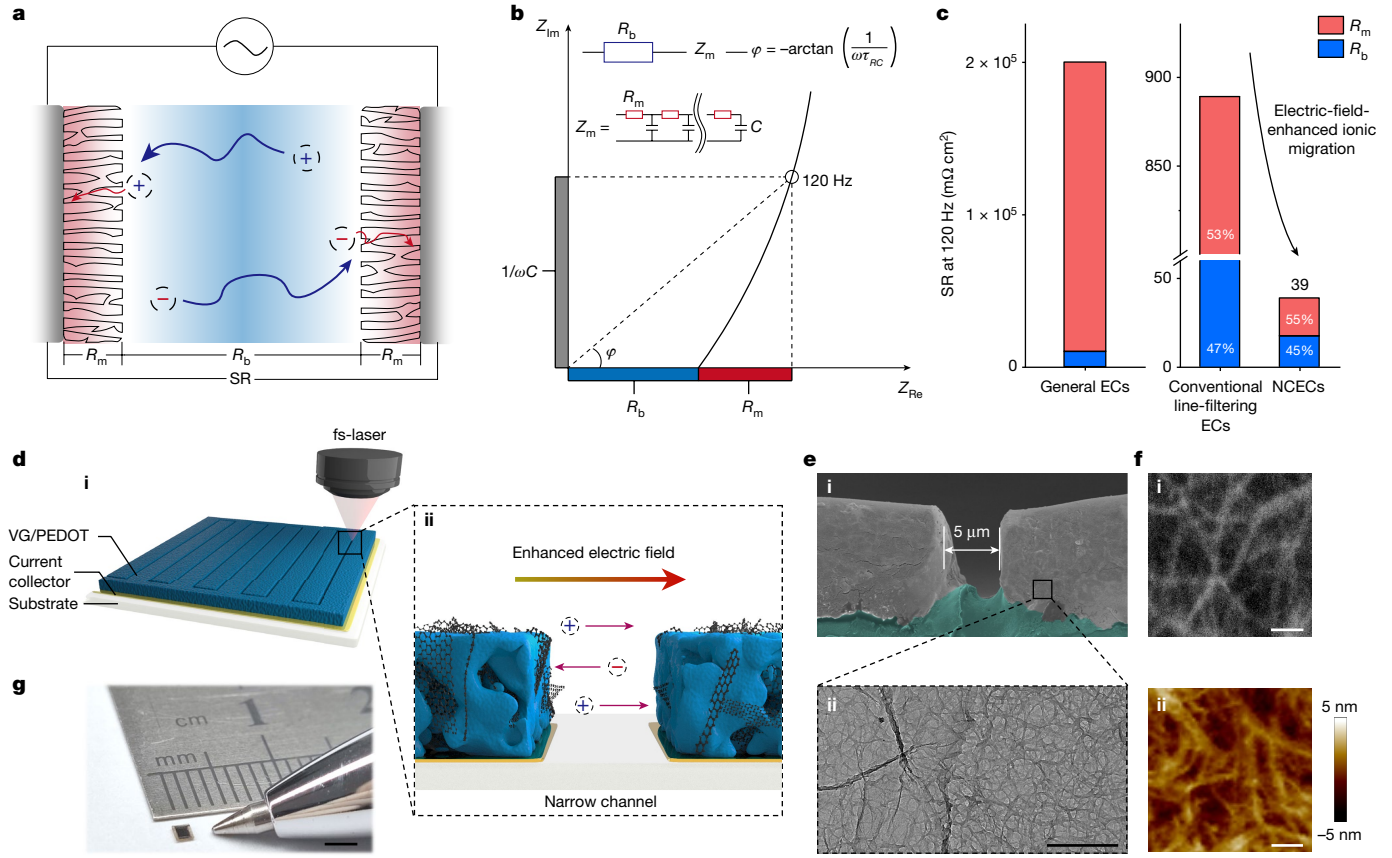

Fig. 1 | Design principle and fabrication of the NCEC. a, Schematic of the constitution of ionic resistance in line-filtering electrochemical capacitors. **b**, Typical Nyquist diagram showing the ionic resistance constitution in the frequency domain. In the formula, φ, ω and τ_{RC} refer to phase angle, angular frequency and RC time constant, respectively. Inset, corresponding equivalent circuit, which is composed of a resistance R_b (blue region) and an impedance Z_m (red region). Z_m corresponds to a transmission-line circuit with R_m and C (capacitance of electrode materials). **c**, Comparison of series resistance at 120 Hz between general electrochemical capacitors, conventional line-filtering electrochemical capacitors and NCECs. **d**, Schematic of the fs-laser scribing process for NCECs (i), and the ionic migration promotion by intense electric field within the narrow channel (ii). **e**, Morphology characterization of NCEC. Cross-sectional false-colour scanning electron microscopy image of the narrow channel between electrodes (i). The turquoise region refers to the current collector and substrate. High-resolution transmission electron microscopy image of the VG/PEDOT film (ii). Scale bar, 200 nm. **f**, Characterization of the mesoporous structure of PEDOT. High-angle annular dark-field scanning transmission electron microscopy (i) and atomic force microscopy images (ii) of PEDOT. Scale bar, 20 nm. **g**, Optical image of NCEC in comparison with the pen point. Scale bar, 2 mm. EC, electrochemical capacitor; SR, series resistance.

between the frequency characteristic and capacitance, the self-induced intense electric field could improve both frequency characteristic and capacitance simultaneously (Extended Data Fig. 1c). By downscaling the channel width using femto-second-laser (fs-laser) scribing (Fig. 1d (i)), we establish an intense electric field in a narrow-channel in-plane line-filtering electrochemical capacitor (NCEC) (Fig. 1d(ii)), resulting in an ultralow series resistance of 39 mΩ cm^2 at 120 Hz. As a consequence, an ultrahigh areal capacitance of up to 5.2 mF cm^{-2} is achieved with a phase angle of −80° at 120 Hz, which is double that of the previously known values[4,13,14].

To fabricate the NCEC, a facile but precise bottom-up processing method is established (Methods). Unlike ordinary fluid-coating techniques, we first fabricate uniformly distributed vertical reduced graphene oxide arrays on current collectors by electrodeposition, which act as anchors to ensure the superwetting behaviour of poly(3,4-ethylenedioxythiophene):poly(styrenesulphonate) (PEDOT:PSS) solution[26,27] (Extended Data Fig. 2a–e). Next, a time-lapse evaporation-induced assembly of PEDOT:PSS is carried out to control the variance of film thickness within 5% (Extended Data Fig. 2f–h). Subsequently, a phase separation occurs in the PEDOT:PSS film by methanol treatment to provide the methanol-treated PEDOT:PSS (VG/PEDOT) film supported by vertical reduced graphene oxide with high electronic conductivity and high-density interconnecting mesoporous structure[28,29] (Fig. 1e,f and Extended Data Fig. 3), which favours the rapid ionic transport and provides abundant ionic storage sites simultaneously. On this basis, by exploiting the fs-laser with ultrahigh transient energy density, specific patterns are written directly by instantaneous gasification without excessive heat damage[30–32]. With a depth of more than 10 μm, channel downscaling to 5 μm is constructed in the NCECs (Fig. 1e (i)). After attaching the grate and adding the electrolyte, a delicate individual NCEC with a miniaturized size smaller than a pen point is established (Fig. 1g and Extended Data Fig. 4a–d).

Electrochemical performances of NCECs

We evaluate the frequency characteristic of the NCECs using electrochemical impedance spectroscopy (EIS). As shown in Fig. 2a, the Nyquist curve is nearly perpendicular to the abscissa axis, indicating the fast and unhindered ionic migration. Meanwhile, the NCEC shows an ultralow series resistance of 39 mΩ cm^2 at 120 Hz. Compared with other in-plane and sandwich-type line-filtering electrochemical capacitor values reported previously[3–5], the total series resistance of the NCEC is reduced by an order of magnitude and towards a minimum level (Extended Data Fig. 4e and Supplementary Table 1, 2). The ultralow series resistance

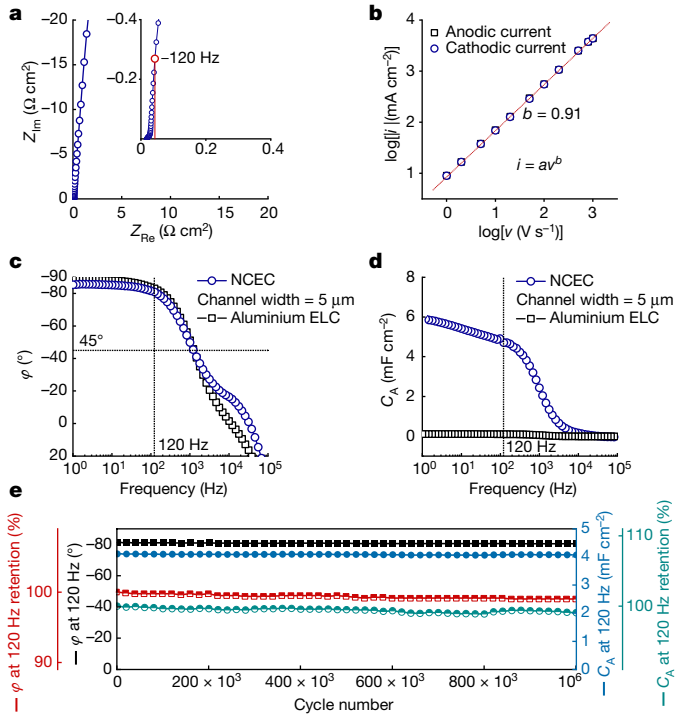

Fig. 2 | Electrochemical performances of the NCEC. a, Nyquist diagram of the NCEC. Inset, high-frequency part. The red point indicates the impedance at 120 Hz. **b**, Logarithmic plots of anodic and cathodic currents (i) versus the logarithm of scan rates (v) for the NCEC. The b value is determined from the slope of the plots. **c**, Bode plots of the NCEC and commercial aluminium ELC, respectively. **d**, Plots of areal capacitance versus frequency of the NCEC and commercial aluminium ELC, respectively. **e**, Stability of areal capacitance and phase angle at 120 Hz with a long-term GCD test of the NCEC over 1 million cycles.

is in tandem with the ultrafast ionic kinetic behaviour, as shown by the scant polarization observed in cyclic voltammetry tests. A kinetic parameter b determined from the power-law relationship is fitted to the cathodic current at different scanning rates from 1 V s^{-1} to 1,000 V s^{-1} (Fig. 2b). Here, b = 0.91 for the NCEC is close to 1, indicating a typical ultrafast capacitive behaviour with unimpeded ionic migration[33,34].

The ultralow series resistance also enables an excellent trade-off between fast responses and capacitance. As τ_{RC} is controlled below 0.2 ms with increasing VG/PEDOT thickness, the areal capacitance can be greatly improved with φ below −80° (Supplementary Fig. 1). As shown in Fig. 2c,d, the NCEC has a comparative φ with commercial aluminium ELC (Nippon Chemi-con), indicating its excellent fast response. By contrast, the areal capacitance of the NCEC is far superior to that of the aluminium ELC, reaching an ultrahigh level of 5.2 mF cm^{-2}, and outperforming other in-plane and sandwich-type line-filtering electrochemical capacitors at all ranges, nearly double the previous record[4,13,14] (Extended Data Fig. 4f and Supplementary Table 3). Moreover, continuous galvanostatic charge and discharge (GCD) test is conducted for more than a million cycles. No obvious performance degradation emerges for the capacitance and phase angle at 120 Hz (Fig. 2e), verifying the excellent reliability of the NCECs for long-term running.

Mechanism of series resistance reduction

We experimentally investigated the impact of the electric field on series resistance by exploiting the channel width as the typical control variable (see detailed analysis on other geometrical parameters in Supplementary Figs. 1–3). As shown in Fig. 3a,b, when the channel width narrows down from 40 μm to 5 μm, R_b and R_m at 120 Hz show the same descending tendency, changing from 43 mΩ cm^2 to 17 mΩ cm^2 and from 79 mΩ cm^2 to 21 mΩ cm^2, respectively. Accordingly, the fast responses get better with phase angle decreasing from −79° to −82° at 120 Hz, and the areal capacitance increases from 2.5 mF cm^{-2} to 4.5 mF cm^{-2} (Fig. 3c).

First-principles and kinetic Monte Carlo calculations are combined to simulate the multi-scale system and uncover the underlying mechanism (Fig. 3d). First, as for the high-frequency-dominated R_b, the behaviour of the system is independent of the kinetic evolution at 120 Hz but correlates with the external electric field (**E**) intensity and intrinsic ionic mobilities (u) of the electrolytes. The simulated results demonstrate that the external **E** within the channels is vastly increased with the downscaling of the channel width (Fig. 3e and Supplementary Fig. 4). The enhanced external **E** acts as the driving force to boost the electromigration (**r**) in the electrolyte (**r** = u × **E**), which accounts for the drastic reduction in R_b.

Furthermore, the kinetic Monte Carlo simulation shows the full-process information about the ionic migration in the low-frequency region (Extended Data Fig. 5). Under varying external voltage, the hindrance of ionic migration renders the hysteresis behaviour of built-in voltage with respect to external voltage, which is verified both in simulation and in experiments (Fig. 3f and Extended Data Fig. 6). Analysis of the hysteresis shows that the simulated R_m decreases with downscaling channel width, which is consistent with the experimental EIS results (Fig. 3g). To investigate the microscopic mechanism, the effective **E** considering the screen effect of stored ions at states 1–3 are depicted separately (Fig. 3h). Compared with the 40-μm channel width, the effective **E** in the case of the 5-μm channel width is generally higher, especially at state 3. In this situation, the effective **E** is markedly suppressed by the screening of stored ions in the 40-μm case, whereas the downscaling channel can greatly enhance the effective **E** near the channel. Meanwhile, the fluorescence tracing results are in accordance with the simulation, showing faster ionic migration in the NCEC in the 5-μm channel (Supplementary Fig. 5 and Supplementary Video 1). Thus, the enhanced **E** considerably promotes the ionic migration, which accounts for the lessened hysteresis (Fig. 3f) and reduced R_m.

Furthermore, the increase in areal capacitance can also be clarified: (1) More electrode materials are available with the occupation of channels being cut down. (2) The ions can reach more storage sites within the same time frame. As demonstrated by the ionic density distribution (Fig. 3i), more ions migrate in a cycle in the case of the 5-μm device, whereas for the 40-μm device, some ions are stuck in the electrode materials because of the insufficient driving force to overcome the adsorption (Extended Data Fig. 5b). Based on the detailed depiction of the wholistic kinetic process, the simulated tendency of resistance and capacitance is consistent with that of the experiments (Extended Data Fig. 5c,d).

Scalable integration of the NCECs

Integration is important for the broadening of capacitance range and voltage window for on-demand customization, but, so far, scalable high-density integration with unit consistency remains unachieved[4,5,11,12,24,25,35]. Taking advantage of the fs-laser scribing, the NCEC units in a specific pattern can be fabricated within seconds. After the attachment of the grate and addition of electrolyte, an integrated NCEC microcircuitry (INM) with a density of up to 80 cells cm^{-2} is established, which features miniaturization and even flexibility (Fig. 4a and Extended Data Fig. 7). Taking the 6 × 6 INM (six modules made of six seriated units connected in parallel) as an example, each NCEC unit is 1 × 1 mm^2. The holistic 6 × 6 INM takes up only 6.7 × 6.7 mm^2 in area and 0.11 mm in height, much smaller than the fingertip (Fig. 4b). Moreover, the performance uniformity of the component units is imperative to the successful integration because the insufficient capacitance of a unit causes its overloading of partial voltage, resulting in holistic damage. Benefiting from the device

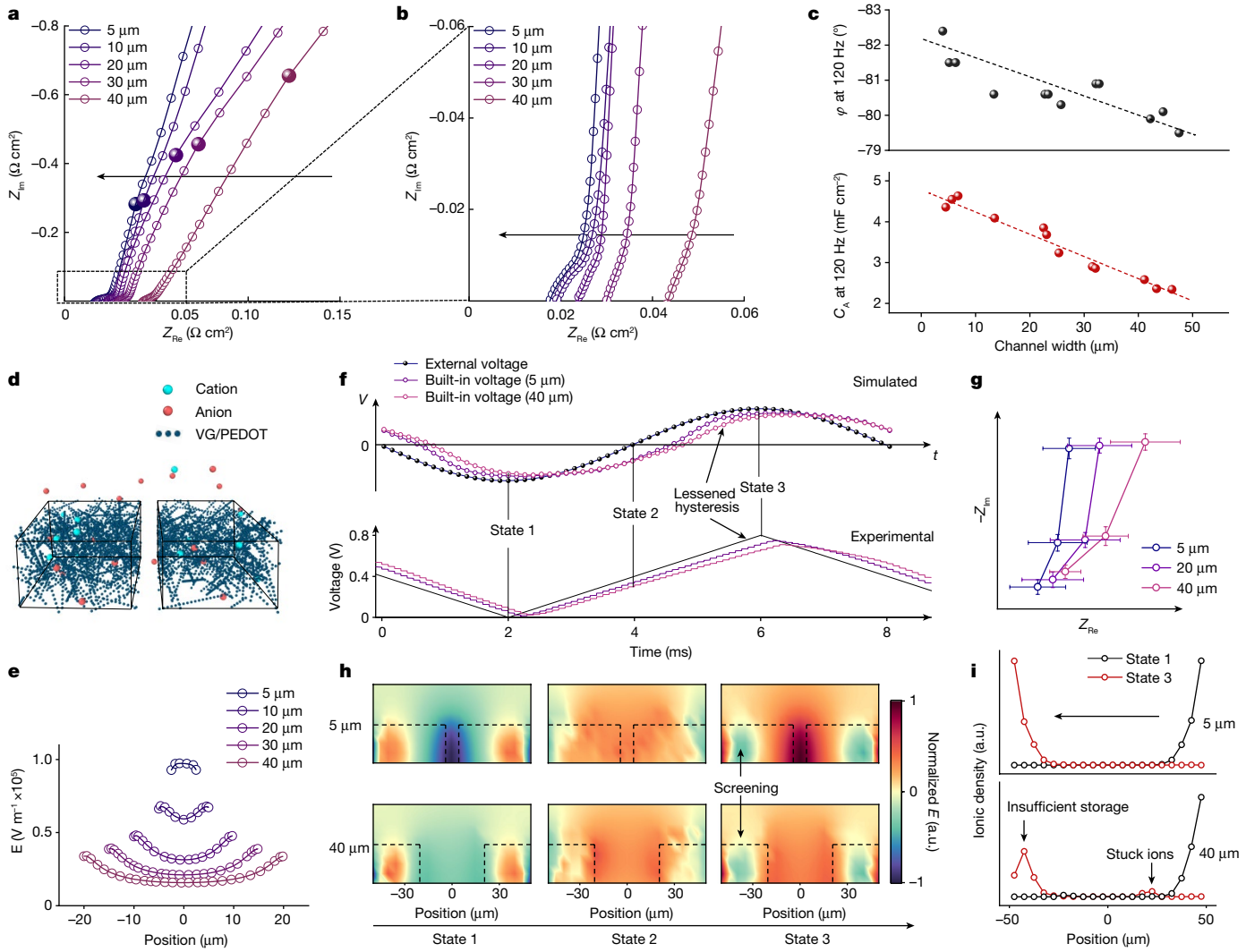

Fig. 3 | Underlying mechanism of series resistance reduction in the NCECs. **a**,**b**, Nyquist diagram (**a**) and its high-frequency part (**b**) of the NCECs with different channel widths. The solid dots in **a** indicate the impedances at 120 Hz, in which the abscissa refers to series resistance and ordinates to $1/\omega C$. The arrow indicates the descending tendency of the channel width. **c**, The phase angle (top) and areal capacitance (bottom) of the NCECs with different channel widths at 120 Hz. The dashed line indicates the variation tendency. **d**, Schematic of the simulated coarse-grain model of the NCEC with the 5 μm channel in kinetic Monte Carlo simulation. **e**, The calculated electric-field intensity within the channels of different widths at the static external voltage of 1 V. **f**, The whole-process information of built-in voltage varying with external voltage in the NCECs with the 5 μm and 40 μm channels, including the simulated results (top) and the experimental results (bottom). **g**, The simulated Nyquist diagram of the NCEC with the 5 μm, 20 μm and 40 μm channels ($n = 10$, error bars indicate standard deviation). **h**, The simulated effective electric field in the NCEC of the 5 μm and 40 μm channels at state 1 to state 3 in **f**. The dashed line indicates the profile of the channel and electrodes. **i**, The simulated ionic density distribution of the NCEC with the 5 μm (top) and 40 μm (bottom) channel widths at state 1 and state 3. The arrow indicates the ionic flow direction. a.u., arbitrary units.

consistency, the capacitance difference between the NCEC units is limited to within 10% (Fig. 4c), which ensures the deviation of partial voltage and phase angle at 120 Hz below 5% and 10%, respectively (Fig. 4d). More than 200,000 cycles of GCD test validates the long-term reliability of the INM (Extended Data Fig. 8).

To investigate the feasibility of on-demand integration for specific performances, a single NCEC, six NCECs in series, six NCECs in parallel and a 6 × 6 INM are prepared and tested (Supplementary Figs. 6 and 7). As shown in Fig. 4e,f, the INMs and the single NCEC possess identical phase angles at 120 Hz and relaxation time, indicating the same fast-response ability. This can be attributed to the constant τ_{RC} despite different integration types, which originates from the rational integration protocol and device consistency (Supplementary Fig. 8). More importantly, the high integration degree endows the INMs with high device volumetric capacitance of up to 0.38 F cm^{-3} V^{-2}, outperforming other line-filtering electrochemical capacitors reported previously[4,35]. Compared with the commercial ELCs, including aluminium ELCs (Nippon Chemi-Con), tantalum ELCs (AVX) and polymer aluminium ELCs (Murata), the INMs take full advantage of device volume with voltage below 35 V (Fig. 4g and Supplementary Table 4). Moreover, ultrahigh volumetric capacitance of up to 10 F cm^{-3} V^{-2} is demonstrated based on solely VG/PEDOT, suggesting that the higher performance of INMs could be achieved by integration optimization.

Performance in line-filtering circuits

As a prototype of line filtering for integrated circuits, a field test in a printed circuit board (PCB)-grade switching circuit is conducted (Fig. 4h). First, the NCECs show a substantial advantage in size over the ELCs with the same capacitance. As shown in Fig. 4i, a single NCEC occupies less than 1/10th footprint of an aluminium ELC (47 μF, 4 V, Nippon Chemi-Con). On integration, a 2 × 10 INM has the same voltage

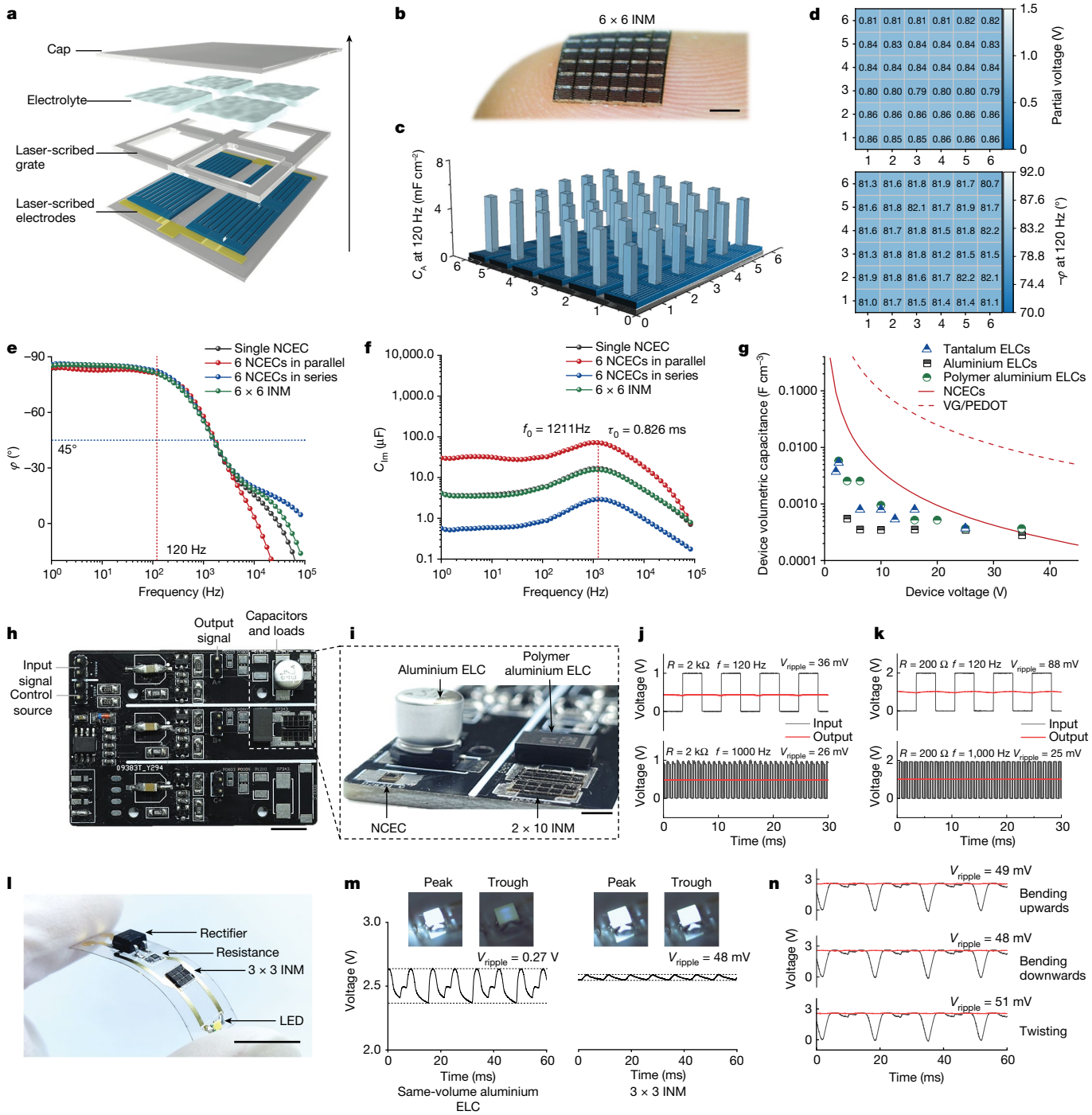

Fig. 4 | Scalable integration of the NCECs and performances in line-filtering circuits. a, Schematic of the scalable high-density integration procedure of the NCECs. **b**, Optical image of the 6 × 6 INM on a fingertip. Scale bar, 2 mm. **c**, Areal capacitance at 120 Hz of each NCEC unit within the 6 × 6 INM. **d**, Partial voltages (top) and phase angles (bottom) at 120 Hz of each NCEC unit within the 6 × 6 INM. **e**, Plots of phase angle versus frequency for a single NCEC and INMs. **f**, Plots of imaginary part of capacitance versus frequency for a single NCEC and INMs. **g**, Comparison of device volumetric capacitance between the NCECs and ELCs. The red dashed line indicates the volumetric capacitance solely based on the VG/PEDOT film. **h**, Optical image of the switching PCB. Scale bar, 5 mm. **i**, Comparison of volume between the NCECs and ELCs. A single NCEC, an aluminium ELC, a 2 × 10 INM (ten modules made of two seriated units connected in parallel) and a polymer aluminium ELC are attached to the board. Scale bar, 2 mm. **j**, Oscillograms of voltage signals filtered by a single NCEC at 120 Hz (top) and 1,000 Hz (bottom) with 2 kΩ load resistance. **k**, Oscillograms of voltage signals filtered by a 2 × 10 INM at 120 Hz (top) and 1,000 Hz (bottom) with 200 Ω load resistance. **l**, Optical image of the flexible circuit, which is composed of a rectifier, resistance, 3 × 3 INM and an LED light bead. Scale bar, 1 cm. **m**, Oscillograms of voltage signals of the flexible circuit, including that filtered by the same-volume aluminium ELC (left) and a 3 × 3 INM (right), respectively. Inset, high-speed optical images of the LED light bead at peaks and troughs of the voltage signal. **n**, Oscillograms of the voltage signals of the flexible circuits at upward bending (top), downward bending (middle) and twisting (bottom) states.

rating and capacitance as the aluminium ELC (220 μF, 2 V, Murata), but a much smaller size (1.7 mm^3 versus 60 mm^3). Second, the NCECs outperform the ELCs with the same volume in line-filtering ability. With 2 kΩ load resistance (0.5 mA load current), a single NCEC can filter a voltage signal from 1 V to 0.5 V at 120 Hz, with the ripple voltage (V_{ripple}) down to 36 mV. Meanwhile, a 1,000 Hz signal filtering can also

be realized with a V_{ripple} of only 26 mV (Fig. 4j). By contrast, aluminium ELCs of this small size failed in filtering and V_{ripple} reached 613 mV and 117 mV, respectively. Furthermore, customized integration of NCECs could meet the requirements of various circuits. For a load current of up to 5 mA with a load resistance of 200 Ω, a 2 × 10 INM can afford line filtering with V_{ripple} below 88 mV and 25 mV for a frequency of 120 Hz and 1,000 Hz, respectively, whereas the V_{ripple} values of aluminium ELC with the same volume are 1,144 mV and 242 mV, respectively (Fig. 4k and Extended Data Fig. 9). Owing to the excessive series resistance and limited capacitance, previous line-filtering electrochemical capacitors fail in filtering such a large current (Supplementary Table 5). By contrast, the NCECs can reduce V_{ripple} down to less than 5%, sufficient for common integrated circuits and far exceeding the commercial ELCs in size.

Furthermore, the NCECs can be integrated into a typical flexible circuit (Fig. 4l). A customized 3-V voltage window is guaranteed by configuring a 3 × 3 INM, and a stroboscopic light emitting diode (LED) is designated as an appliance and indicator, the flickering of which can be caught by a high-speed camera to visually indicate the signal fluctuation. In contrast to the vast light flickering by using the same-volume aluminium ELC as filter, the 3 × 3 INM controls V_{ripple} to within 50 mV (<2%) and the intensity of LED light is steady (Fig. 4m). Meanwhile, benefiting from the flexibility, consistency and stability of each unit, short circuit and conductivity decay are avoided[17] (Extended Data Fig. 10). As a result, the 3 × 3 INM exhibits excellent and consistent filtering performances when being bent or even twisted, well qualified for the next-generation portable flexible electronics (Fig. 4n and Supplementary Video 2).

Conclusion

In summary, we propose an electric-field enhancement strategy to promote ionic migration both in the electrode material and electrolyte. By downscaling the channel width with fs-laser scribing, we present NCECs with an ultralow series resistance of down to 39 mΩ cm^2 at 120 Hz. Consequently, the areal capacitance of up to 5.2 mF cm^{-2} is achieved with a phase angle of −80° at 120 Hz, which is double the previously known values[4,13,14]. Scalable and high-density integration of NCECs provide the INM with a high integration density of 80 cells cm^{-2}, excellent circuit compatibility and on-demand customization of capacitance and voltage. This work takes an important step forward in the practical implementation of line-filtering electrochemical capacitors and provides an opportunity for the development of miniaturized microcircuits and next-generation flexible electronics.

Online content

Any methods, additional references, Nature Portfolio reporting summaries, source data, extended data, supplementary information, acknowledgements, peer review information; details of author contributions and competing interests; and statements of data and code availability are available at https://doi.org/10.1038/s41586-023-06712-2.

1. Miller, J. R., Outlaw, R. A. & Holloway, B. C. Graphene double-layer capacitor with ac line-filtering performance. *Science* **329**, 1637–1639 (2010).
2. El-Kady, M. F., Strong, V., Dubin, S. & Kaner, R. B. Laser scribing of high-performance and flexible graphene-based electrochemical capacitors. *Science* **335**, 1326–1330 (2012).
3. Pech, D. et al. Ultrahigh-power micrometre-sized supercapacitors based on onion-like carbon. *Nat. Nanotechnol.* **5**, 651–654 (2010).
4. Han, F. et al. Structurally integrated 3D carbon tube grid-based high-performance filter capacitor. *Science* **377**, 1004–1007 (2022).
5. Wu, M. et al. Arbitrary waveform AC line filtering applicable to hundreds of volts based on aqueous electrochemical capacitors. *Nat. Commun.* **10**, 2855 (2019).
6. Lim, J. et al. Dopant-specific unzipping of carbon nanotubes for intact crystalline graphene nanostructures. *Nat. Commun.* **7**, 10364 (2016).
7. Wu, Z. S., Parvez, K., Feng, X. & Mullen, K. Graphene-based in-plane micro-supercapacitors with high power and energy densities. *Nat. Commun.* **4**, 2487 (2013).
8. Xu, S. et al. Vertical graphene arrays as electrodes for ultra-high energy density ac line-filtering capacitors. *Angew. Chem. Int. Ed.* **60**, 24505–24509 (2021).
9. Park, J. & Kim, W. History and perspectives on ultrafast supercapacitors for ac line filtering. *Adv. Energy Mater.* **11**, 2003306 (2021).
10. Fan, Z., Islam, N. & Bayne, S. B. Towards kilohertz electrochemical capacitors for filtering and pulse energy harvesting. *Nano Energy* **39**, 306–320 (2017).
11. Qi, D., Liu, Y., Liu, Z., Zhang, L. & Chen, X. Design of architectures and materials in in-plane micro-supercapacitors: current status and future challenges. *Adv. Mater.* **29**, 1602802 (2017).
12. Ye, J. et al. Direct laser writing of graphene made from chemical vapor deposition for flexible, integratable micro-supercapacitors with ultrahigh power output. *Adv. Mater.* **30**, 1801384 (2018).
13. Zhang, M. et al. Bridged carbon fabric membrane with boosted performance in AC line-filtering capacitors. *Adv. Sci.* **9**, 2105072 (2022).
14. Li, W., Azam, S., Dai, G. & Fan, Z. Prussian blue based vertical graphene 3D structures for high frequency electrochemical capacitors. *Energy Storage Mater.* **32**, 30–36 (2020).
15. Suran, J. J. & Marolf, R. A. Integrated circuits and integrated systems. *Proc. IEEE* **52**, 1661–1668 (1964).
16. Wang, F. et al. Latest advances in supercapacitors: from new electrode materials to novel device designs. *Chem. Soc. Rev.* **46**, 6816–6854 (2017).
17. Rangom, Y., Tang, X. & Nazar, L. F. Carbon nanotube-based supercapacitors with excellent ac line filtering and rate capability via improved interfacial impedance. *ACS Nano* **9**, 7248–7255 (2015).
18. Kyerematen, N. A., Brousse, T. & Pech, D. Microsupercapacitors as miniaturized energy-storage components for on-chip electronics. *Nat. Nanotechnol.* **12**, 7–15 (2017).
19. Yan, J., Li, S., Lan, B., Wu, Y. & Lee, P. S. Rational design of nanostructured electrode materials toward multifunctional supercapacitors. *Adv. Funct. Mater.* **30**, 1902564 (2019).
20. Zhong, C. et al. A review of electrolyte materials and compositions for electrochemical supercapacitors. *Chem. Soc. Rev.* **44**, 7484–7539 (2015).
21. Wang, X. et al. Probing nanoconfined ion transport in electrified 2D laminate membranes with electrochemical impedance spectroscopy. *Small Methods* **6**, 2200806 (2022).
22. Chi, F. et al. Graphene ionogel ultra-fast filter supercapacitor with 4 V workable window and 150 °C operable temperature. *Small* **18**, 2200916 (2022).
23. Chi, F. et al. Graphene-based organic electrochemical capacitors for ac line filtering. *Adv. Energy Mater.* **7**, 1700591 (2017).
24. Laszczyk, K. U. et al. Lithographically integrated microsupercapacitors for compact, high performance, and designable energy circuits. *Adv. Energy Mater.* **5**, 1500741 (2015).
25. Jiang, Q. et al. On-chip MXene microsupercapacitors for ac-line filtering applications. *Adv. Energy Mater.* **9**, 1901061 (2019).
26. Liu, M., Wang, S. & Jiang, L. Nature-inspired superwettability systems. *Nat. Rev. Mater.* **2**, 17036 (2017).
27. Tian, Y. & Jiang, L. Intrinsically robust hydrophobicity. *Nat. Mater.* **12**, 291–292 (2013).
28. Alemu, D., Wei, H.-Y., Ho, K.-C. & Chu, C.-W. Highly conductive PEDOT:PSS electrode by simple film treatment with methanol for ITO-free polymer solar cells. *Energy Environ. Sci.* **5**, 9662–9671 (2012).
29. Xia, Y., Sun, K. & Ouyang, J. Solution-processed metallic conducting polymer films as transparent electrode of optoelectronic devices. *Adv. Mater.* **24**, 2436–2440 (2012).
30. Kerse, C. et al. Ablation-cooled material removal with ultrafast bursts of pulses. *Nature* **537**, 84–88 (2016).
31. Gattass, R. R. & Mazur, E. Femtosecond laser micromachining in transparent materials. *Nat. Photonics* **2**, 219–225 (2008).
32. Yang, W., Kazansky, P. G. & Svirko, Y. P. Non-reciprocal ultrafast laser writing. *Nat. Photonics* **2**, 99–104 (2008).
33. Augustyn, V. et al. High-rate electrochemical energy storage through Li+ intercalation pseudocapacitance. *Nat. Mater.* **12**, 518–522 (2013).
34. Chen, W. et al. Two-dimensional quantum-sheet films with sub-1.2 nm channels for ultrahigh-rate electrochemical capacitance. *Nat. Nanotechnol.* **17**, 153–158 (2022).
35. Wang, J., Li, F., Zhu, F. & Schmidt, O. G. Recent progress in micro-supercapacitor design, integration, and functionalization. *Small Methods* **3**, 1800367 (2018).

Methods

Preparation of materials

Preparation of graphene oxide. Graphene oxide dispersion was synthesized through the modified Hummers's method[36] at low temperatures to reduce structural defects. Typically, 20 g of deionized water was mixed with ice-cooled 230 ml H_2SO_4 (98 wt%) at 0 °C under 400 rpm mechanical stirring, followed by the addition of 5 g graphite powder (325 mesh, Qingdao Huatai lubricant sealing S&T). Next, 15 g of $KMnO_4$ (Sinopharm Chemical Reagent) was carefully and slowly added to the above solution within 1 h. Then, the mixture was kept reacting at 0 °C for 48 h. Next, the mixture was poured into 1,500-ml ice-cooled deionized water, and 30 wt% H_2O_2 solution (Sinopharm Chemical Reagent) was added subsequently to quench the reaction until no bubbles emerged. Before dialysis (cut off: 8,000–14,000 Da, Viskase MD77, 2 weeks), the above mixture was filtered and washed with HCl solution (1 mol l^{-1}) three times. Finally, the purified graphene oxide suspension was obtained by centrifugation at 2,000 rpm and 8,000 rpm, sequentially. For the consequent synthetic steps, the graphene oxide sheets were torn apart into small-sized graphene oxide sheets by ultrasonication for 30 min with Branson Digital Sonifier SFX 250.

Preparation of substrate film. The substrate film consisted of a 30-μm-thick polyethylene terephthalate (PET) film purchased from Shenzhen Huananxiangcheng Technology and an evaporated Au layer as a current collector. The PET film was first washed thoroughly with deionized water and ethanol and was set as a substrate for electronic beam evaporation (L-400EK, ANELVA). A 5-nm thick titanium layer was first deposited as a bonding layer, followed by the deposition of a 200-nm thick Au layer.

Preparation of grate or cap film. The grate or cap film was constructed of a stretchable adhesive layer (3 M 9458) and PET film. First, the double-side adhesive layer was attached to a release liner, exposing the other side for the attachment of cleansed PET film. Desired patterns were obtained by laser scribing (LAJAMIN 3D laser). When being used, the grate or cap film can be transferred from the release liner to the target substrate.

Fabrication of the VG/PEDOT film. First, the vertical reduced graphene oxide array was formed by electrodeposition according to previous reports[37]. The as-prepared graphene oxide was diluted and mixed with $LiClO_4$ (Aladdin) into a 2 mg ml^{-1} graphene oxide and 0.1 M $LiClO_4$ solution as electrolyte. By using a large-area Au plate as a counter-electrode and Ag/AgCl (CHI 111) as a reference electrode, the vertical reduced graphene oxide was deposited on the substrate film at −1.1 V versus Ag/AgCl. After rinsing with deionized water to remove excessive graphene oxide sheets, deep reduction of the vertical reduced graphene oxide was conducted at −1.2 V versus Ag/AgCl in 1 M $LiClO_4$ solution. After dialysis to remove the residual ions, the vertical reduced graphene oxide was formed. Thereafter, the hydrophobic surface of the Au current collector changed to a superhydrophilic surface. Second, a time-lapse evaporation-induced assembly of PEDOT:PSS film on the vertical reduced graphene oxide array was conducted to fabricate the VG/PEDOT:PSS film. When the surplus water on the surface was removed but the wetting state remained, the PEDOT:PSS solution (Clevios PH-1000) was drop-cast on the vertical reduced graphene oxide surface, forming a flat and uniform liquid layer. Then the film was located in a flat petri dish parallel to the ground. A slow evaporation process was guaranteed by putting the cap on the petri dish to maintain the vapour pressure at a high level. Thus, the slow assembly speed can be controlled by the slow leakage of vapour, which leads to the uniform assembly of PEDOT:PSS on the vertical reduced graphene oxide array. Next, the VG/PEODT film was obtained by immersing the VG/PEDOT film in methanol solution for 1 min followed by natural drying.

Materials characterization

SEM images were obtained using Hitachi SU-8010 scanning electron microscope. TEM and HADDF-STEM images were obtained by FEI TecnaiTF20 transmission electron microscope. AFM images were acquired using Bruker Dimension Icon atomic force microscope in peak force tapping mode. The WLI morphology was obtained by Zygo NeXView three-dimensional white-light interferometer. The electronic conductivity was tested by a four-point probe setup (GZKD KDY-1). X-ray photoelectron spectroscopy was conducted on ULVAC-PHI PHI Quantro SXM X-ray photoelectron spectrometer. Raman spectrum was obtained using the HORIBA Evolution Raman spectrometer. Optical images were acquired on ZEISS Axio Scope, A1 microscope, RY605 microscope and Canon EOS 80D digital single-lens reflex.

Thickness measurement of the VG/PEDOT film. For the thickness measurement of one point at the VG/PEDOT film, cross-sectional SEM images can be used to get the exact result. For multiple points test in a region of the VG/PEDOT film, the film was first formed on a silicon wafer with roughness less than 1 nm. Next, some of VG/PEDOT was scribed out by laser to form a grid pattern. Because the damage threshold of VG/PEDOT was much smaller than that of the silicon wafer, terraces were formed. Thickness values were then obtained by WLI morphology.

NCEC, INM and line-filtering circuit fabrication

Construction of NCEC. First, ultra-narrow channels were constructed by femtosecond-laser scribing (Uptek phidia-C, frequency = 1,000 Hz, wavelength = 800 nm and power density = 2.5×10^4 W cm^{-2}). The laser scribes out some of the electrode material and Au current collector at the specified position but not the substrate, thus forming the desired patterns. The grate was then attached to the above, surrounding the interdigital region. Next, 3 M H_2SO_4 solution was added as an electrolyte in the middle of the enclose (Extended Data Fig. 4). The channel width can be controlled by the scribing pattern of the femtosecond laser.

Construction of INM. Similar to the construction of NCEC, the INM fabrication also followed a bottom-up procedure. After the preparation of substrate and VG/PEDOT, the specified patterns according to the integration type were formed by laser scribing. After attaching the grate, electrolyte and top sealing, an INM was established (see stepwise schematic diagrams in Extended Data Fig. 7). For INMs, 3 M H_2SO_4, 5% polyvinyl alcohol solution was used as a semi-gel electrolyte to ensure immobility.

Construction of the PCB-grade switching circuit. According to the typical CPU direct current (d.c.) power supply circuit (d.c.–d.c. converter), a prototype switching circuit was constructed with a controlling integrated circuit, triodes and resistances (see the detailed circuit diagram in Extended Data Fig. 9a). NCECs and INM were attached to the PCB by a silver conducting paste (SPI 05002-AB). The d.c. input signal was generated by an arbitrary function generator (Keysight 33500B). With a duty ratio equal to 50% and a frequency of 120 Hz and 1,000 Hz, the signals were filtered by the NCEC and INM with loading resistance of 500 Ω and 200 Ω, respectively.

Construction of the flexible stroboscopic circuit. The flexible stroboscopic circuit consisted of a LED light bead, a full wave rectifier and a load resistor (Extended Data Fig. 10a). Specifically, the substrate was made of PET, and the conductor layer was made of Au. A 3 × 3 INM filter was anchored on the substrate by a silver conducting paste. The input was a sinusoidal signal (60 Hz) generated by the arbitrary function generator. With a loading resistance of 500 Ω, the rectified signals with a peak-to-peak voltage of 2.8 V were filtered by the 3 × 3 INM. The stroboscopic light was recorded by a high-speed camera (Vision Research Phantom v.611).

Device characterization

Electrochemical measurements. Electrochemical performances were measured at the electrochemical workstation (CHI 660e and AMETEK PARSTAT 3000 A). During the test, the environmental humidity was controlled at 50 ± 5% relative humidity and the temperature was controlled at 25 ± 1 °C. Cyclic voltammetry was tested with a scanning rate varying from 1 V s^{-1} to 2,000 V s^{-1}. The GCD was tested at a current density varying from 0.5 mA cm^{-2} to 5 A cm^{-2}. For the long-term stability test, GCD with a current density of 100 mA cm^{-2} was used, and the EIS test was performed at the interval of every 10,000 cycles. For the test of each unit in INM, a probe station (Motic PSM-1000) was used to contact the NCECs.

EIS measurements. The EIS test was conducted by an electrochemical workstation (CHI 660e and AMETEK PARSTAT 3000 A). The initial voltage was 0 V, amplitude was 5 mV, and frequency range varied from 10,000 Hz to 1 Hz, with 12 testing points per decade frequencies.

Electrochemical performance calculations. Based on the data from electrochemical and EIS measurements, the performance parameters were derived according to other reports on line-filtering electrochemical capacitors[1–8].

The real and imaginary parts of capacitance were calculated as

$$C_{\mathrm{Re}}(f) = \frac{-Z_{\mathrm{Im}}(f)}{2\pi M f\,|Z(f)|^2},$$

$$C_{\mathrm{Im}}(f) = \frac{Z_{\mathrm{Re}}(f)}{2\pi M f\,|Z(f)|^2},$$

where $C_{\mathrm{Re}}(f)$ and $C_{\mathrm{Im}}(f)$ are the real and imaginary parts of capacitance at a specified frequency f and $Z_{\mathrm{Re}}(f)$ and $Z_{\mathrm{Im}}(f)$ are the real and imaginary parts of impedance $Z(f)$ at a specified frequency f, which is typically 120 Hz. M is the area or volume of the NCECs. For areal capacitance $C_{\mathrm{A}}(f) = C_{\mathrm{Re}}(f)$, M refers to all the area occupied, including electrodes and channels; for volumetric capacitance $C_{\mathrm{V}}(f) = C_{\mathrm{Re}}(f)$, M refers to all the volume occupied, including electrodes and channels; and for the calculation of device volumetric capacitance $C_{\mathrm{Vvol}}(f) = C_{\mathrm{Re}}(f)/v_{\mathrm{d}}^2$, M refers to all the volume occupied by all components of the device, v_{d} is the voltage rating of the device.

The relaxation time constant τ_0 is determined by $\tau_0 = 1/f_0$, where f_0 is the frequency when $C_{\mathrm{Im}}(f)$ reaches its maximum value.

The ripple voltage V_{ripple} is the peak–peak difference of the voltage signal, and the ripple factor is determined by $V_{\mathrm{ripple}}/V_{\mathrm{input}}$, where V_{input} is the input voltage.

Oscillogram measurements. Oscillograms were recorded by Rohde & Schwarz RTB2002, d.c. mode, with a sampling rate of 83,300 samples per second.

Fluorescence tracing of the ionic migration. Sodium fluorescein solution (0.1 mM) was used as the electrolyte. The fluorescein anion has negative charges and can be excited using 450 nm light, with emission at 520 nm. Thus, by applying cyclic voltammetry with a scan rate of 2 V s^{-1}, we used an optical microscope to observe the corresponding 1 Hz oscillation of fluorescence (Supplementary Fig. 5a).

Detection of the built-in voltage. As shown in Extended Data Fig. 6, we used the probe station to perform the experiment. The two probes were immersed in the thin layer of electrolyte and placed in the middle of the separate opposite interdigital electrodes near the surface of the electrodes without contact. By applying cyclic voltammetry with a scan rate of 200 V s^{-1} (about 120 Hz) on the tested NCEC, the built-in voltage was acquired.

Theoretical calculation

Finite-element analysis. We used the COMSOL software to conduct the simulation of the external electric field in the NCECs. Physical fields of electrostatics and electric currents were used. Conductivity was 500 S cm^{-1} for VG/PEDOT and 220 mS cm^{-1} for the electrolyte. THe dielectric constant was 80 for VG/PEDOT and 78 for the electrolyte[38–40]. First, for the calculation of the holistic electric potential distribution and electric-field intensity distribution, the model was established as completely identical to the realistic NCEC (Supplementary Fig. 4a,b). For the detailed electric-field intensity distribution within the channels, one pair of opposite electrodes was constructed according to the symmetry. For the boundary conditions, according to the experiments, the bottom surface of one electrode was assigned as 0 V and the opposite as 1 V. The cases of channel width varying from 5 μm to 40 μm were calculated, and the corresponding areal resistances were acquired by Ohm's law.

First-principles calculation. The first-principles calculations were implemented using the Vienna Ab initio Simulation Package[41,42]. The exchange-correlation potential was described by the Perdew–Burke–Ernzerhof functional with generalized gradient approximation[43]. The plane wave energy cutoff was set at 400 eV, and the structural relaxations were done with the residual Hellman–Feynman force less than 10^{-3} eV $Å^{-1}$. The convergence of electronic self-consistent was 10^{-5} eV.

The calculation model applied to study the electric potential distribution is shown in Supplementary Fig. 4e, in which the electrodes were composed of PEDOT and graphene layers. The interspacing d and layers n were designated as variables to study the interspacing distance and thickness dependence of the electric potential distribution.

Kinetic Monte Carlo simulation. The N-Fold Way algorithm was applied to perform the kinetic Monte Carlo simulations. Details about this kinetic Monte Carlo and the N-Fold Way algorithm can be found in refs. 44–46. The rate of a diffusional hop is

$$r_{\mathrm{D}} = \begin{cases} D_0 & \Delta E \le 0, \\ D_0 \exp\left(-\dfrac{\Delta E}{k_{\mathrm{B}}\mathrm{T}}\right) & \Delta E > 0, \end{cases}$$

where ΔE represents the energy change induced by the hop. The total energy of our coarse-grain model is given by

$$E_{\mathrm{tot}} = \alpha \sum_{i,j=\mathrm{ions}} \frac{Z_i Z_j}{r_{ij} + d_{\mathrm{c}}} + \sum_j Z_j V_{\mathrm{ext}} + E_{\mathrm{ad}} \sum_k n_k,$$

where the first term is used to describe the interaction between the ions and Z_i represents the charge quantity of the ith ion ($1e$ or $-1e$ in simulations). Its only difference from the Coulomb potential comes from d_c, which is set to guarantee that the Coulomb attraction at the time of collision of the ions is small enough to be broken by the kinetic energy (k_{B}T; where k_{B} is the Boltzmann constant, and T is the temperature). Note that this is a coarse-grain model; the values of d_c and α used in our simulation are set to 1 μm and 0.01 eV μm e^{-2}. The second term represents the energy of ions under the external electric field, where V_{ext} is the electric potential given by two electrodes with uniform charge density (2.88×10^{-6} e μm^{-3}). Moreover, the PEDOT network is considered as a rigid skeleton, and the ions could be adsorbed if the distance between the ions and the PEDOT sites is no more than 1.2 μm, and the adsorption energy E_{ad} is set to −0.18 eV.

For the impedance calculation, the built-in voltage could be monitored in kinetic Monte Carlo simulations by calculating the electric

potential difference at the bottom centre of the electrodes at each step. It is proportional to the charge number accumulating at the electrodes, and thus its partial derivative with respect to x could reflect the dynamic evolution of the electric current. The impedance could be obtained according to its definition—that is, $Z = V/I$, where V and I are the voltage and electric current, respectively, and both of them are complex-valued functions.

Data availability

Additional data related to this work are available from the corresponding authors upon request. Source data are provided with this paper.

Code availability

The code supporting this study is available from the corresponding author upon request.

36. Chen, J. et al. Water-enhanced oxidation of graphite to graphene oxide with controlled species of oxygenated groups. *Chem. Sci.* **7**, 1874–1881 (2016).
37. Sheng, K., Sun, Y., Li, C., Yuan, W. & Shi, G. Ultrahigh-rate supercapacitors based on eletrochemically reduced graphene oxide for ac line-filtering. *Sci Rep.* **2**, 247 (2012).
38. Mansour, A. E. et al. Conductive polymer work function changes due to residual water: impact of temperature-dependent dielectric constant. *Adv. Electron. Mater.* **6**, 2000408 (2020).
39. Koch, N., Vollmer, A. & Elschner, A. Influence of water on the work function of conducting poly(3,4-ethylenedioxythiophene)/poly(styrenesulfonate). *Appl. Phys. Lett.* **90**, 043512 (2007).
40. Bertolini, D., Cassettari, M. & Salvetti, G. The dielectric relaxation time of supercooled water. *J. Chem. Phys.* **76**, 3285–3290 (1982).
41. Kresse, G. & Furthmüller, J. Efficiency of ab-initio total energy calculations for metals and semiconductors using a plane-wave basis set. *Comput. Mater. Sci.* **6**, 15–50 (1996).
42. Kresse, G. & Furthmüller, J. Efficient iterative schemes for *ab initio* total-energy calculations using a plane-wave basis set. *Phys. Rev. B* **54**, 11169–11186 (1996).
43. Perdew, J. P., Burke, K. & Ernzerhof, M. Generalized gradient approximation made simple. *Phys. Rev. Lett.* **77**, 3865–3868 (1996).
44. Battaile, C. C. The Kinetic Monte Carlo method: foundation, implementation, and application. *Comput. Methods Appl. Mech. Eng.* **197**, 3386–3398 (2008).
45. Bortz, A. B., Kalos, M. H. & Lebowitz, J. L. A new algorithm for Monte Carlo simulation of Ising spin systems. *J. Comput. Phys.* **17**, 10–18 (1975).
46. Gillespie, D. T. Exact stochastic simulation of coupled chemical reactions. *J. Chem. Phys.* **81**, 2340–2361 (1977).
47. Zhao, D. et al. Charge transfer salt and graphene heterostructure-based micro-supercapacitors with alternating current line-filtering performance. *Small* **15**, 1901494 (2019).
48. Wu, Z. et al. Alternating current line-filter based on electrochemical capacitor utilizing template-patterned graphene. *Sci Rep.* **5**, 10983 (2015).
49. Xu, S., Liu, W., Hu, B. & Wang, X. Circuit-integratable high-frequency micro supercapacitors with filter/oscillator demonstrations. *Nano Energy* **58**, 803–810 (2019).
50. Kurra, N., Jiang, Q., Syed, A., Xia, C. & Alshareef, H. N. Micro-pseudocapacitors with electroactive polymer electrodes: toward ac-line filtering applications. *ACS Appl. Mater. Interfaces* **8**, 12748–12755 (2016).
51. Lin, J. et al. 3-Dimensional graphene carbon nanotube carpet-based microsupercapacitors with high electrochemical performance. *Nano Lett.* **13**, 72–78 (2013).
52. Wu, Z. S. et al. Bottom-up fabrication of sulfur-doped graphene films derived from sulfur-annulated nanographene for ultrahigh volumetric capacitance micro-supercapacitors. *J. Am. Chem. Soc.* **139**, 4506–4512 (2017).
53. Li, Z. et al. Aqueous hybrid electrochemical capacitors with ultra-high energy density approaching for thousand-volts alternating current line filtering. *Nat. Commun.* **13**, 6359 (2022).
54. Kang, Y. J., Yoo, Y. & Kim, W. 3-V solid-state flexible supercapacitors with ionic-liquid-based polymer gel electrolyte for ac line filtering. *ACS Appl. Mater. Interfaces* **8**, 13909–13917 (2016).
55. Zhang, M. et al. Robust graphene composite films for multifunctional electrochemical capacitors with an ultrawide range of areal mass loading toward high-rate frequency response and ultrahigh specific capacitance. *Energy Environ. Sci.* **11**, 559–565 (2018).
56. Wen, Y., Chen, H., Wu, M. & Li, C. Vertically oriented MXene bridging the frequency response and capacity density gap for ac-filtering pseudocapacitors. *Adv. Funct. Mater.* **32**, 2111613 (2022).
57. Zhang, M. et al. An ultrahigh-rate electrochemical capacitor based on solution-processed highly conductive PEDOT:PSS films for AC line-filtering. *Energy Environ. Sci.* **9**, 2005–2010 (2016).
58. Zhang, Z. et al. Scalable fabrication of ultrathin free-standing graphene nanomesh films for flexible ultrafast electrochemical capacitors with AC line-filtering performance. *Nano Energy* **50**, 182–191 (2018).
59. Ren, G., Pan, X., Bayne, S. & Fan, Z. Kilohertz ultrafast electrochemical supercapacitors based on perpendicularly-oriented graphene grown inside of nickel foam. *Carbon* **71**, 94–101 (2014).
60. Yuan, Y. et al. Bottom-up scalable temporally-shaped femtosecond laser deposition of hierarchical porous carbon for ultrahigh-rate micro-supercapacitor. *Sci. China Mater.* **65**, 2412–2420 (2022).
61. Premathilake, D. et al. Fast response, carbon-black-coated, vertically-oriented graphene electric double layer capacitors. *J. Electrochem. Soc.* **165**, A924–A931 (2018).
62. Zhang, C., Du, H., Ma, K. & Yuan, Z. Ultrahigh-rate supercapacitor based on carbon nano-onion/graphene hybrid structure toward compact alternating current filter. *Adv. Energy Mater.* **10**, 2002132 (2020).

Acknowledgements We acknowledge the financial support from the National Science Foundation of China (grant nos. 22035005, 52022051, 52090032, 22075165 and 52073159), State Key Laboratory of Tribology in Advanced Equipment (SKLT) (SKLT2021B03) and the Tsinghua-Foshan Innovation Special Fund (2020THFS0501). F.L. acknowledges support from the National Natural Science Foundation of China (grant nos. 11972349 and 11790292) and the Strategic Priority Research Program of the Chinese Academy of Sciences (grant no. XDB22040503). M.W. acknowledges the financial support from the National Science Foundation of China (grant no. 22105040), the Fujian Science and Technology Innovation Laboratory for Optoelectronic Information of China (grant no. 2021ZZ127) and the Natural Science Foundation of Fujian Province of China (grant no. 2021J01588). We also thank Z. Yu and X. Li from Peking University for their instruction in femtosecond-laser scribing technology and thank B. Yang from the North China Electric Power University for his instruction in constructing the line-filtering circuits.

Author contributions L.Q. supervised the entire project. Y.H., M.W. and L.Q. designed the experiments. Y.H. performed most of the experimental measurements with help from M.W., F. Chi, P.L., W.H., B.L., C.W., F. Chen and H.C. L.J. gave advice on experiments. Y.H., J.L., G.L. and F.L. conducted theoretical simulation. Y.H. prepared the paper with advice from M.W., F.L. and L.Q. All authors discussed the results and reviewed the paper.

Competing interests The authors declare no competing interests.

Additional information

Supplementary information The online version contains supplementary material available at https://doi.org/10.1038/s41586-023-06712-2.

Correspondence and requests for materials should be addressed to Liangti Qu.

Peer review information *Nature* thanks the anonymous reviewers for their contribution to the peer review of this work.

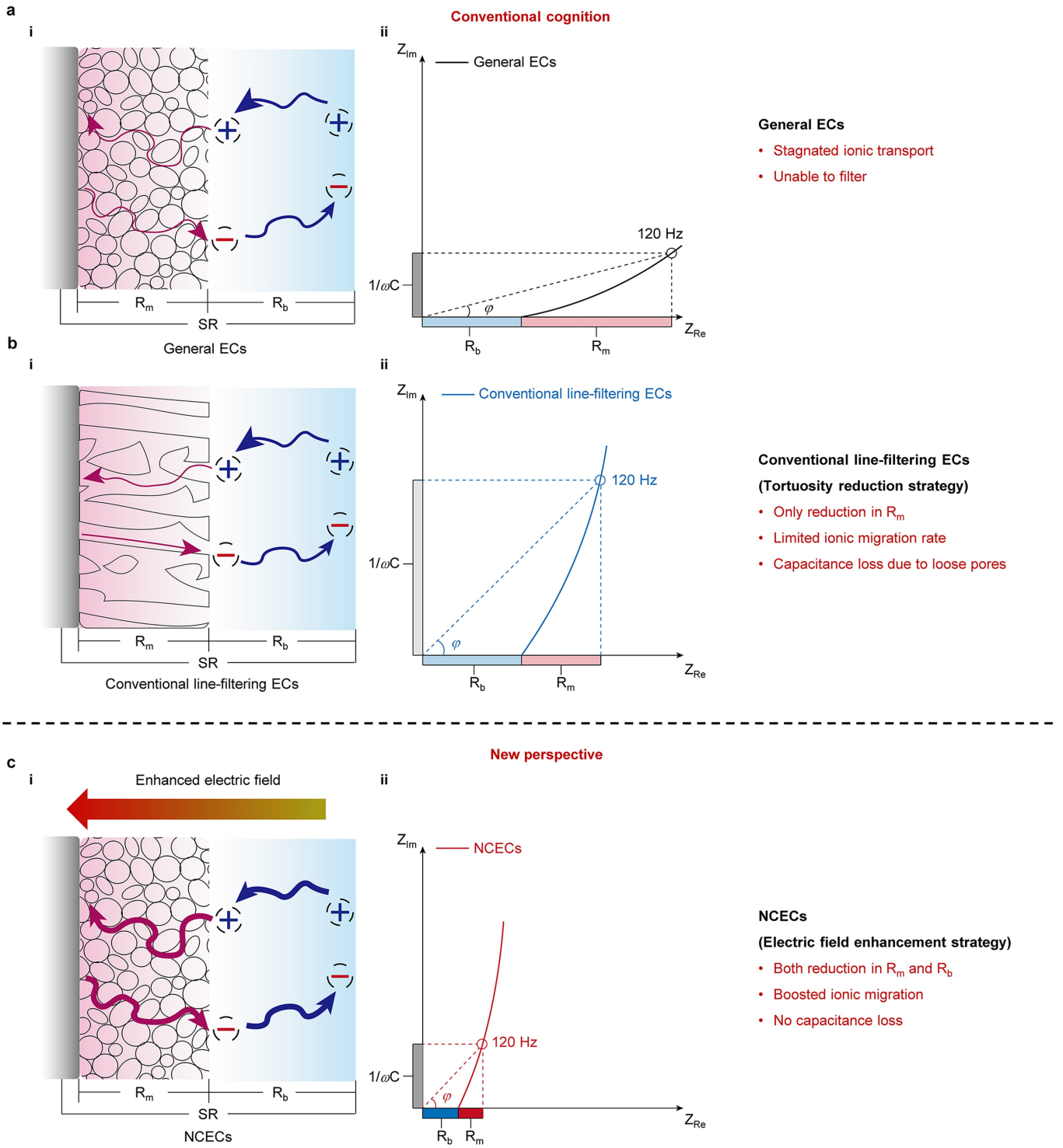

Extended Data Fig. 1 | Comparison of designing strategies between NCECs with conventional electrochemical line-filtering ECs. a–**c**, The schematic diagrams of designing strategies in general ECs (**a**), conventional line-filtering ECs (**b**), and NCECs (**c**). The subsequence numbers **i** and **ii** refer to the schematic diagrams of structural design and the corresponding typical Nyquist diagram, separately. Please see Supplementary Note 1 for the detailed explanation.

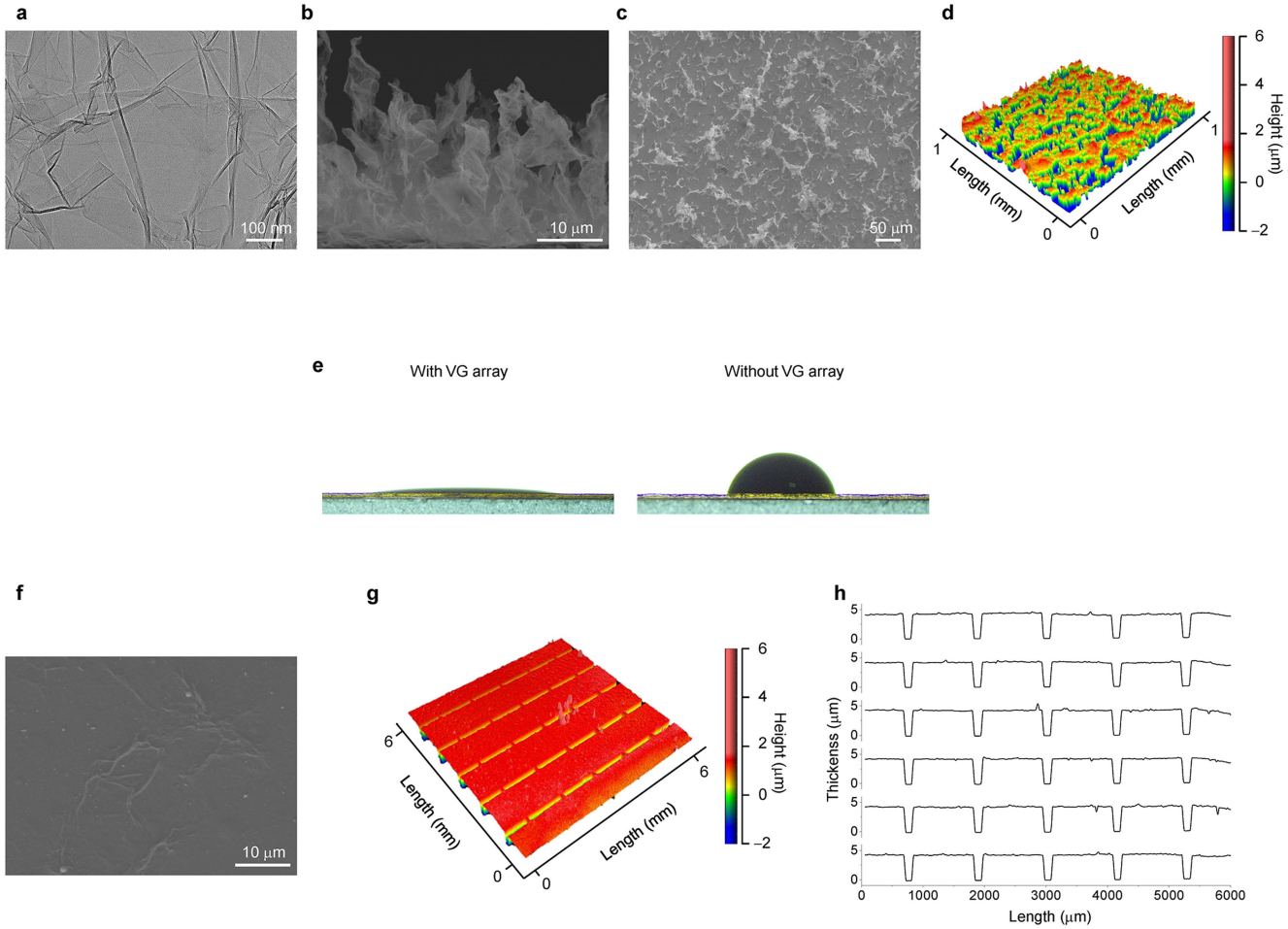

Extended Data Fig. 2 | Characterization of VG array and VG/PEDOT:PSS film. a, High-resolution TEM image of the graphene sheet. **b**,**c**, SEM images of as-fabricated VG array, concerning the lateral view (**b**) and the top view (**c**). **d**, Three-dimensional (3D) white-light interference (WLI) morphological graph of the VG array. **e**, Contact angles to PEDOT:PSS solution droplet for the Au current collector with VG array (left panel) and without VG array (right panel). **f**, SEM image of VG/PEDOT:PSS film from the top view. **g**, 3D WLI morphological graph of the VG/PEDOT:PSS film. **h**, The corresponding detailed thickness information derived by 3D WLI morphological graph in **g**.

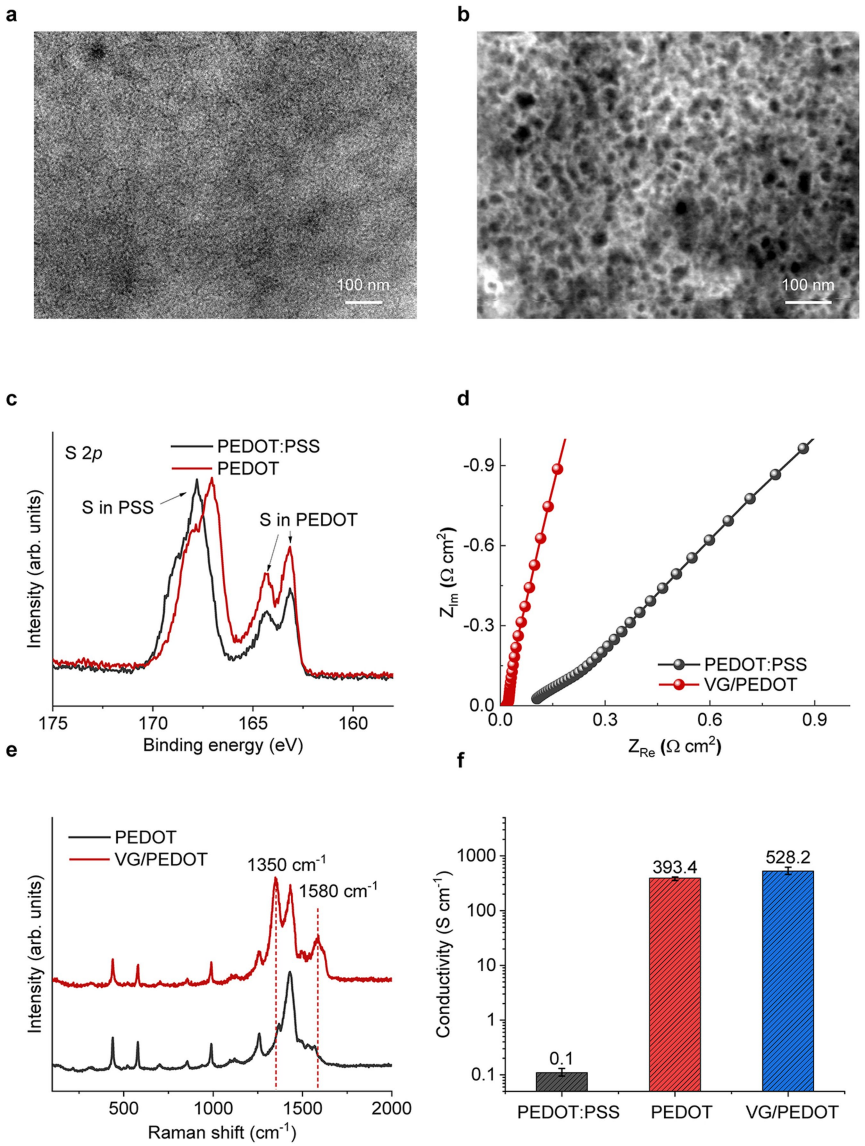

Extended Data Fig. 3 | Impact of methanol treatment on VG/PEDOT film. **a**,**b**, HAADF-TEM images of PEDOT:PSS film (**a**) and PEDOT film (**b**). **c**, S (2*p*) X-ray photoelectron spectroscopy of PEDOT:PSS film and PEDOT film. After methanol treatment, the ratio of S (PSS) to S (PEDOT) changes from 2.18 to 1.52, indicating the decrease of PSS content. **d**, Nyquist diagram of PEDOT:PSS film and VG/PEDOT film. The ascending slope indicates the reduced transmission-line-like behaviour in PEDOT, which results from the enriched mesoporous structure. **e**, Raman spectrum of PEDOT film and VG/PEDOT film. **f**, Conductivity of PEDOT:PSS film, PEDOT film and VG/PEDOT film ($n = 3$; error bars indicate standard deviation).

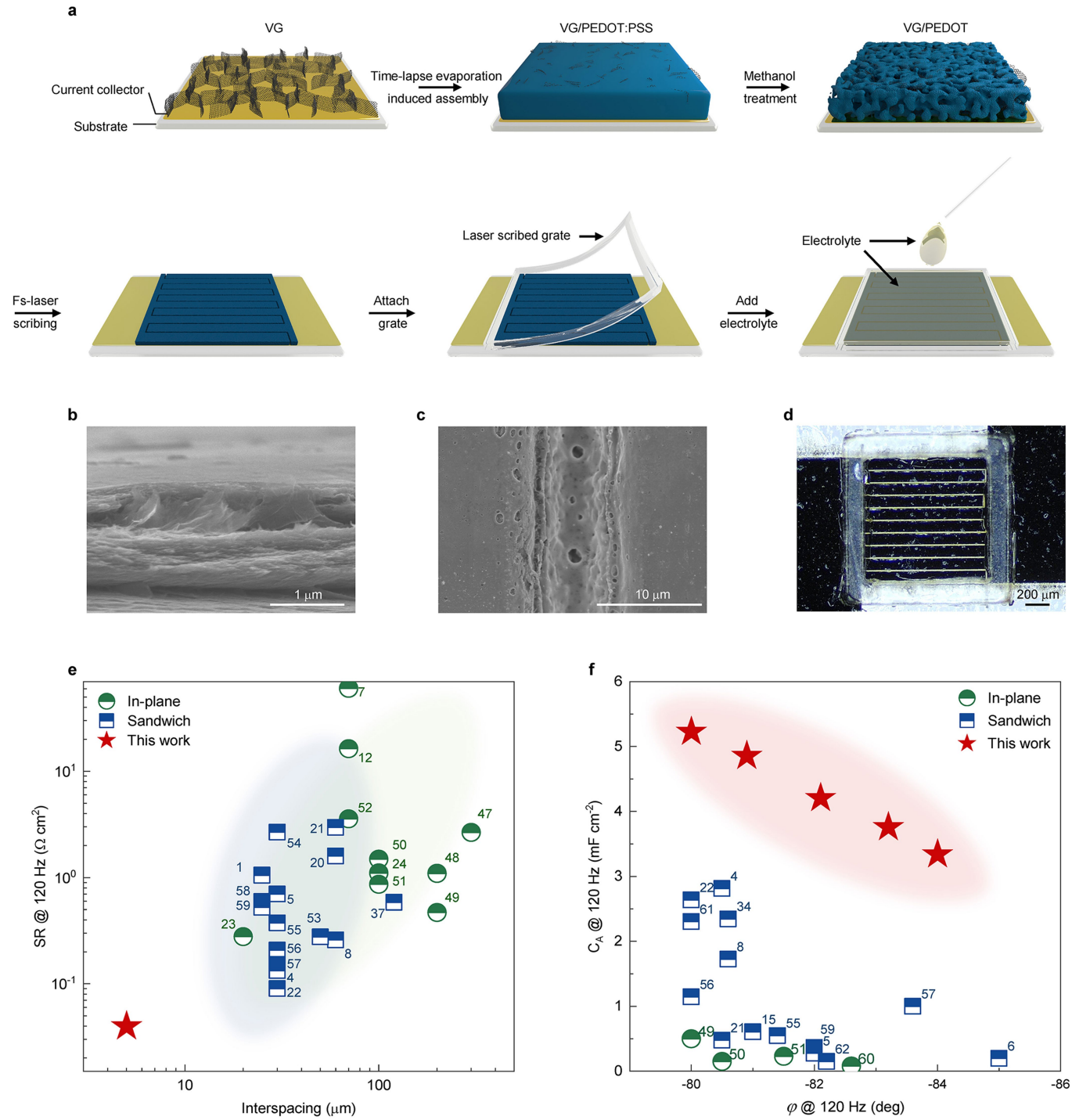

Extended Data Fig. 4 | Fabrication procedure and characterization of NCEC. **a**, Schematic diagram of the fabrication process of NCEC. **b**–**d**, SEM images of as-fabricated NCEC including, the lateral vision of VG/PEDOT film consisting of VG array and PEDOT parts (**b**), the top view of the fs-laser scribed channel (**c**), and the top view of the interdigital electrodes of NCEC. **e**, Comparison of SR and electrode interspacing between NCEC with other in-plane[7,12,24,25,47–52] and sandwich-type[1,4,5,8,13,14,22,23,53–59] line-filtering ECs. The number of the points is the reference number. **f**, Comparison of areal capacitance and phase angle at 120 Hz between NCECs with other in-plane[49–51,60] and sandwich-type[4–6,8,13,14,17,23,55–57,59,61,62] line-filtering ECs. The number of the points is the reference number.

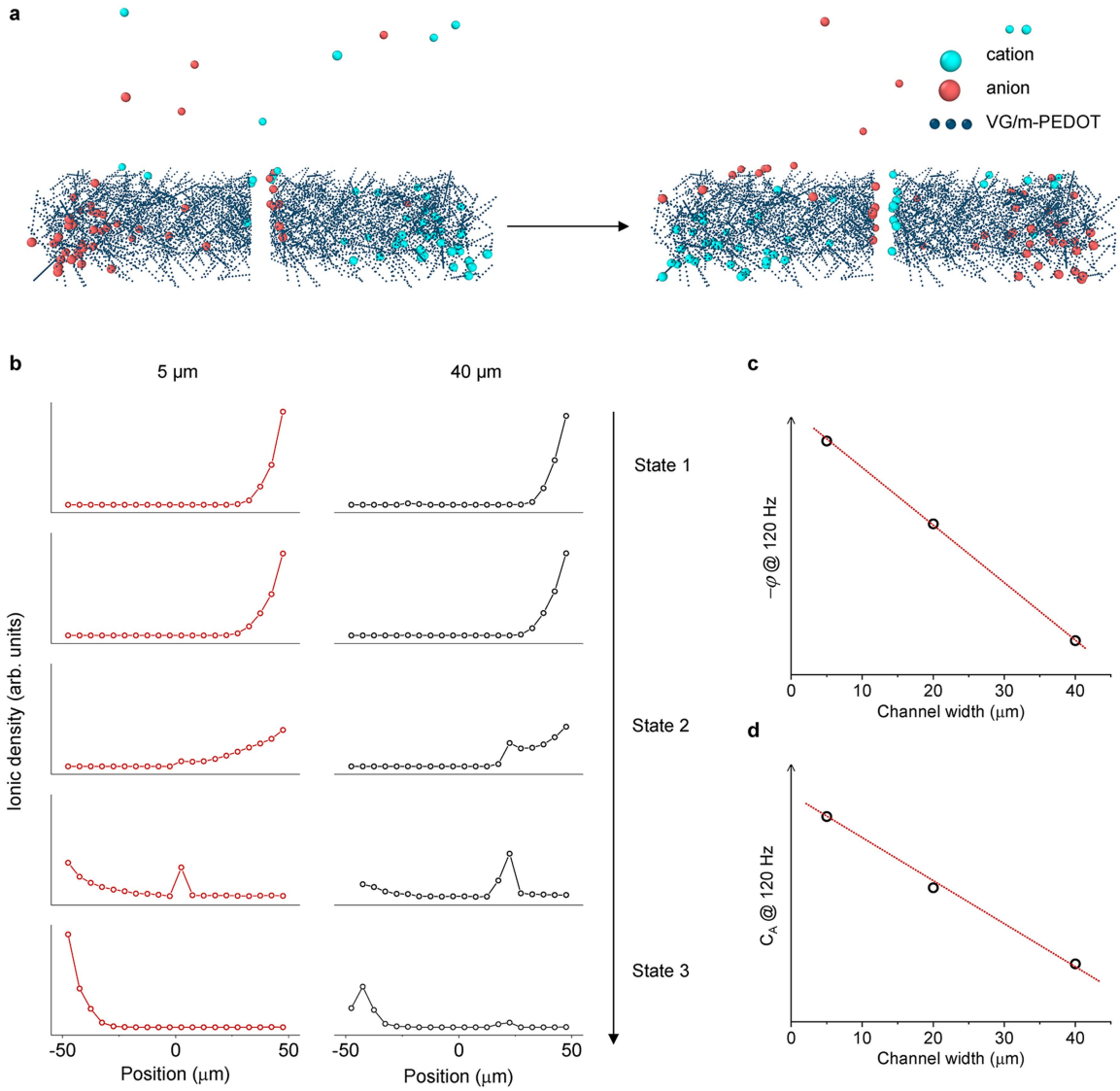

Extended Data Fig. 5 | Whole-process information calculated by kinetic Monte Carlo simulation. a, The simulated kinetic process of ionic migration in NCECs in half a period: from state 1 that all the ions are stored in the left-side electrode (left panel) to state 3 that all the ions are stored in the right-side electrode (right panel). **b**, The stepwise evolution of ionic distribution of the NCEC with channel width of 5 μm (left panel) and 40 μm (right panel) from state 1 to state 3. **c**, The calculated φ of NCECs with different channel width. **d**, The calculated C_A of NCECs with different channel width.

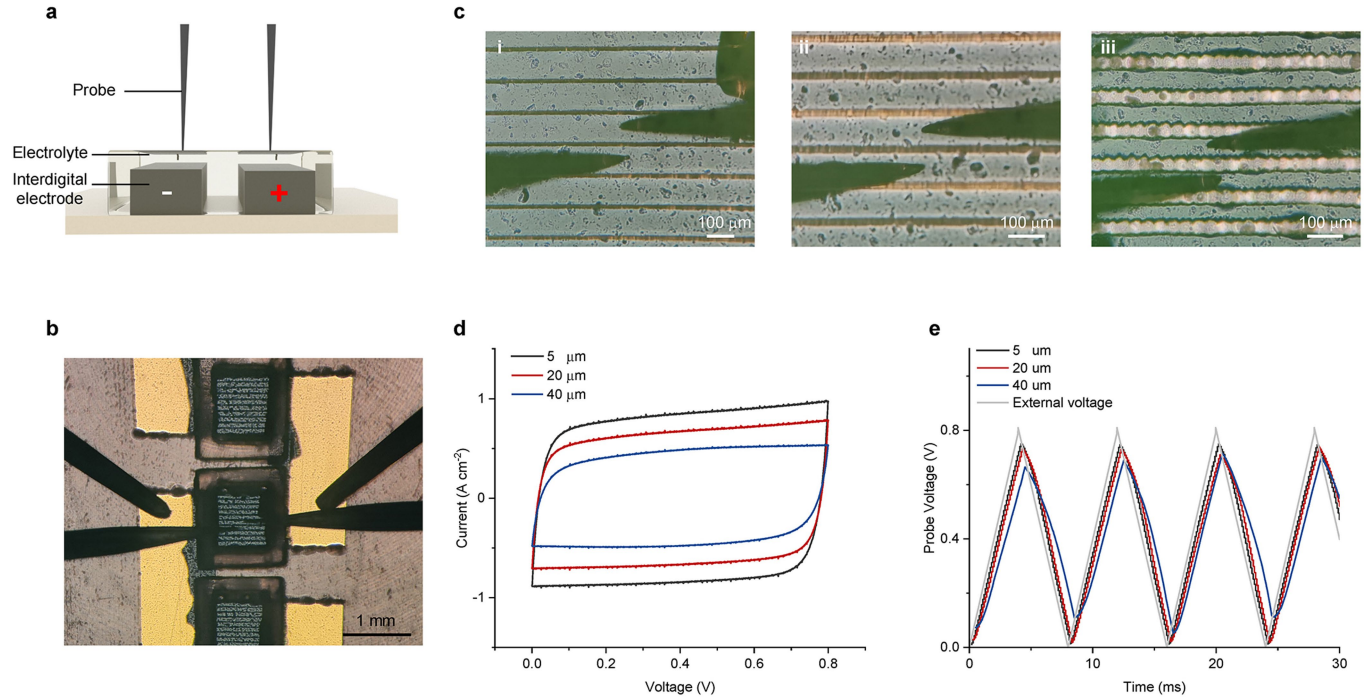

Extended Data Fig. 6 | Detection of built-in voltage. a, Schematic diagram of the experimental apparatus. **b**, Optical microscopic image of the experimental apparatus. **c**, Optical microscopic images of the tested NCECs with channel width of 5 μm, 20 μm and 40 μm. **d**, The cyclic voltammetry of the tested NCECs with channel width of 5 μm, 20 μm and 40 μm. **e**, The built-in voltage signal of the tested NCECs with channel width of 5 μm, 20 μm and 40 μm, varying with external voltage.

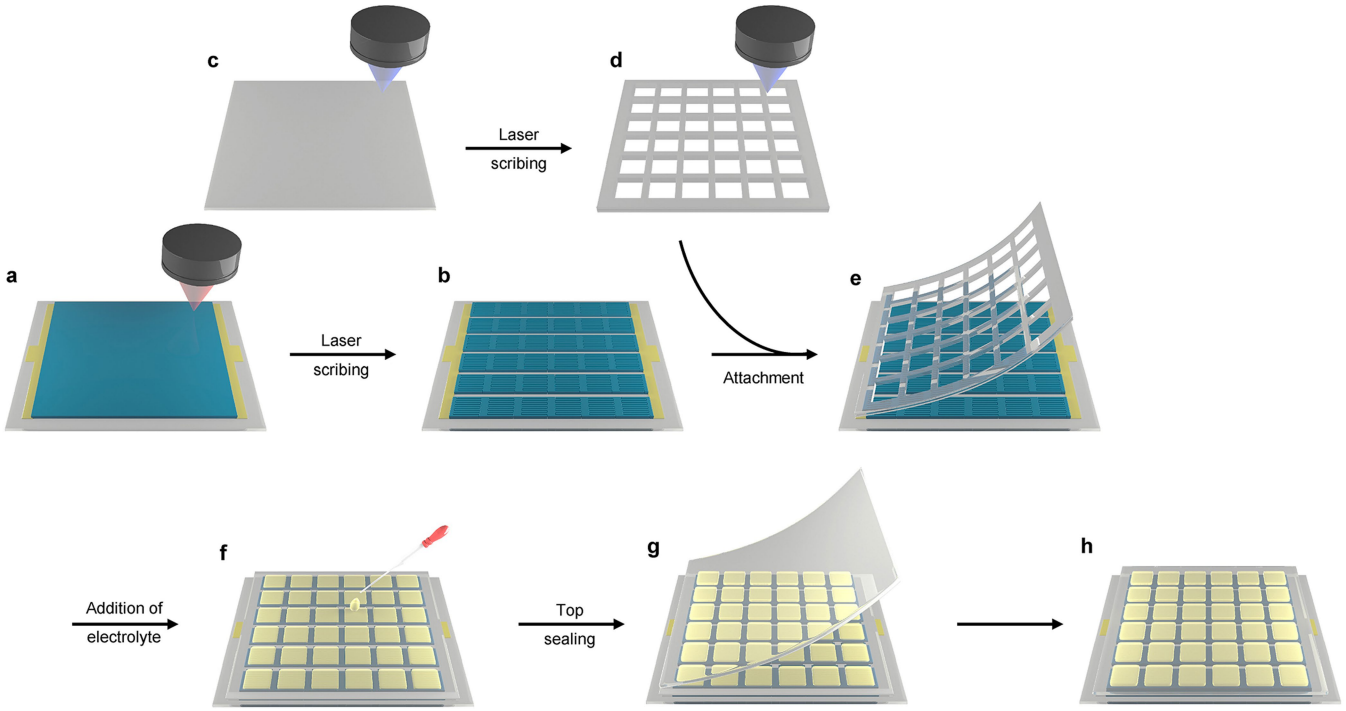

Extended Data Fig. 7 | Schematic diagram of the scalable integration procedure of NCECs. a, Scribing specified patterns and channels by fs-laser **b**, The as-prepared interdigital electrodes array. **c**, Scribing grate by laser. **d**, The as-prepared grate. **e**, Attachment of the grate onto interdigital electrodes array. **f**, Addition of electrolyte. **g**, Attachment of the top sealing cap. **h**, The as-prepared INM.

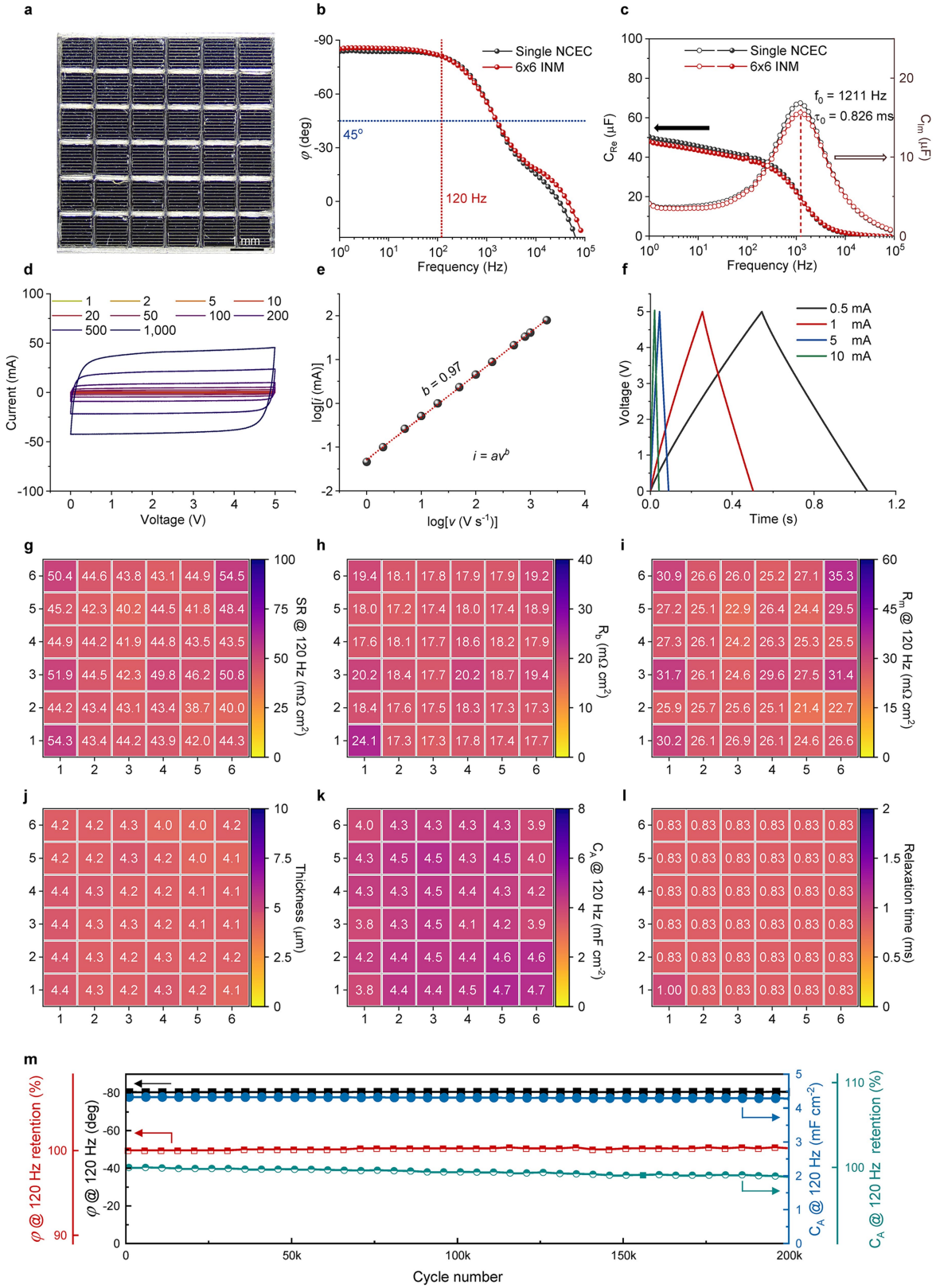

Extended Data Fig. 8 | Electrochemical performances of 6×6 INM. a, Optical microscopic image of 6×6 INM. **b**, Bode diagram of a single NCEC and 6×6 INM. **c**, Plots of real and imaginary part of capacitance versus frequency of a single NCEC and 6×6 INM. **d**, Cyclic voltammetry of 6×6 INM at different scan rates ranging from 1 V s^{-1} to 1,000 V s^{-1}. **e**, Plot of the logarithm of anodic and cathodic currents (i) versus the logarithm of scan rates (v) for 6×6 INM. The b value is determined from the slope of the plots. **f**, GCD curves of 6×6 INM at different current ranging from 0.5 mA to 10 mA. **g**–**l**, Heat map showing electrochemical performances of each NCEC unit in 6×6 INM, including SR at 120 Hz (**g**), R_b (**h**), R_m at 120 Hz (**i**), thickness of VG/PEDOT (**j**), C_A at 120 Hz (**k**), and relaxation time (**l**). **m**, Long-term stability test of 6×6 INM over 200,000 cycles.

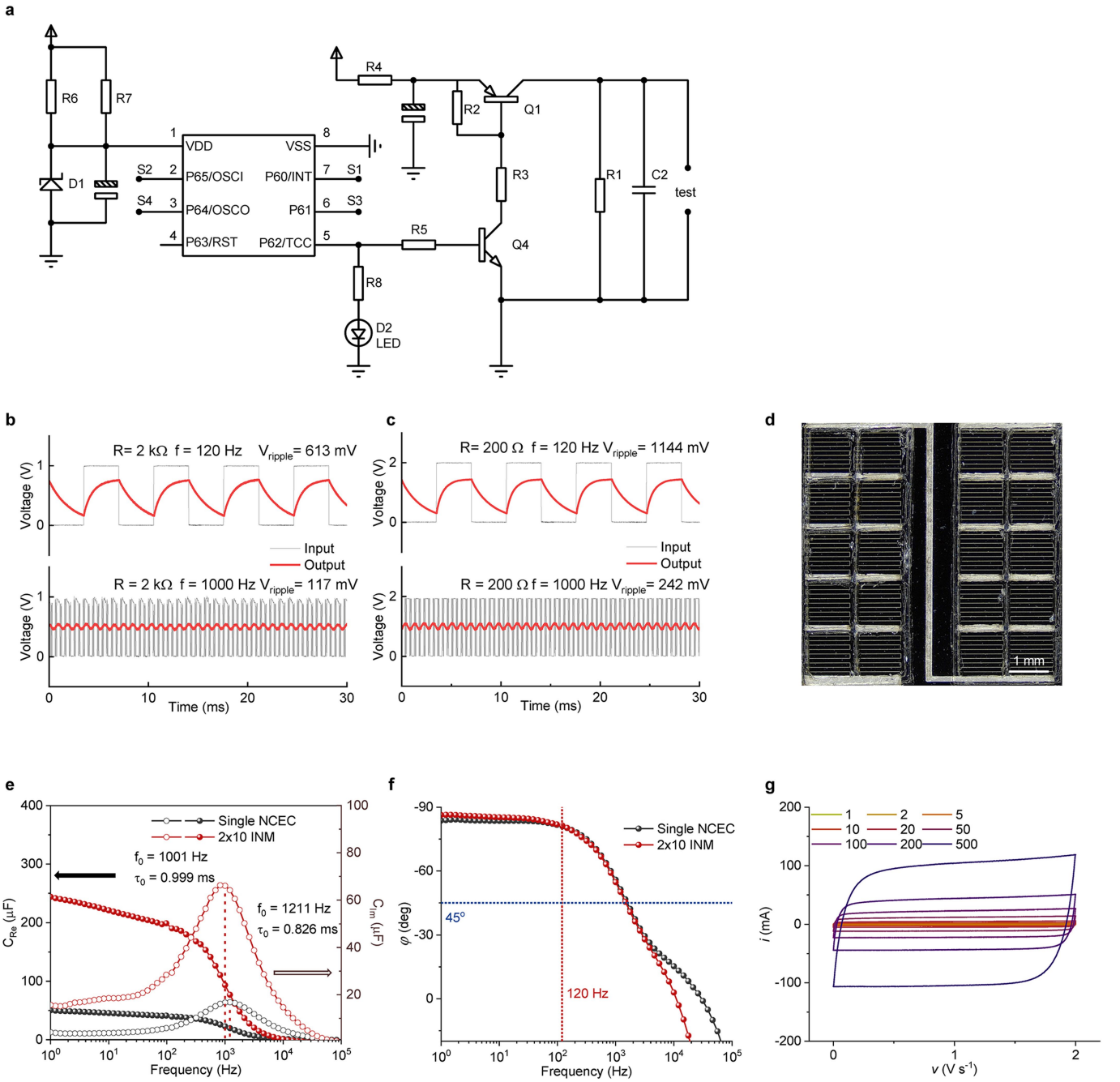

Extended Data Fig. 9 | Line-filtering performances of a single NCEC and 2×10 INM in PCB grade switching circuit. a, Schematic circuit diagram of the switching circuit. **b**, Oscillograms of voltage signals filtered by aluminium ELCs which have the same capacitance as a single NCEC at 120 Hz (upper panel) and 1,000 Hz (bottom panel). **c**, Oscillograms of signals filtered by aluminium ELCs which have the same capacitance as 2×10 INM at 120 Hz (upper panel) and 1,000 Hz (bottom panel). **d**, Optical image of 2×10 INM. **e**, Plots of real and imaginary part of capacitance versus frequency of a single NCEC and 2×10 INM. **f**, Bode diagram of a single NCEC and 2×10 INM. **g**, Cyclic voltammetry of 2×10 INM at different scan rates ranging from 1 V s^{-1} to 500 V s^{-1}.

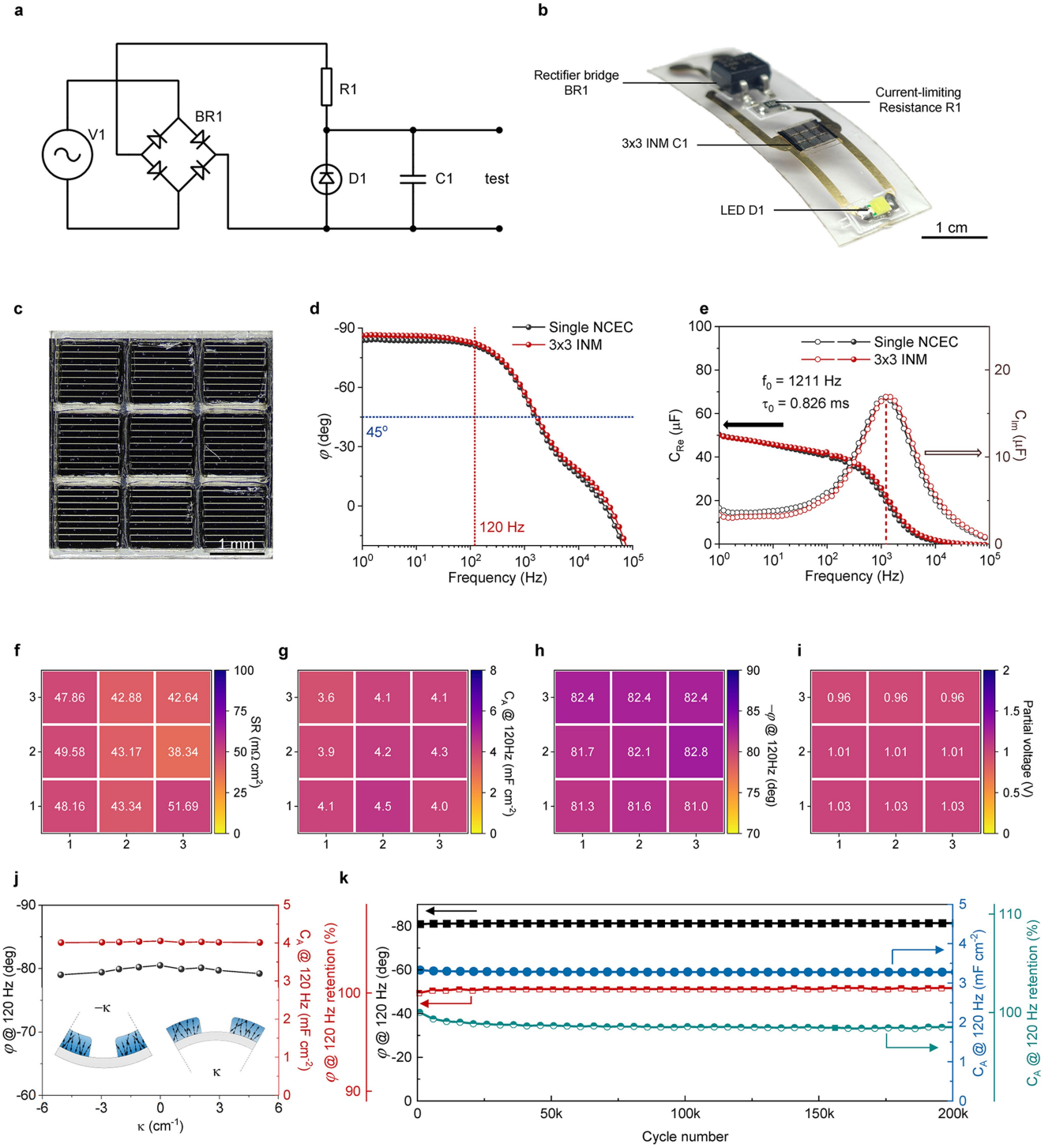

Extended Data Fig. 10 | Line-filtering performances of 3×3 INM in flexible stroboscopic circuit. a, Schematic circuit diagram of the flexible stroboscopic circuit. **b**, Optical image of the flexible PCB. **c**, Optical image of 3×3 INM. **d**, Bode diagram of a single NCEC and 3×3 INM. **e**, Plots of real and imaginary part of capacitance versus frequency of a single NCEC and 3×3 INM. **f**–**i**, Heat map showing electrochemical performances of each NCEC unit in 3×3 INM, including SR at 120 Hz (**f**), C_A at 120 Hz (**g**), φ at 120 Hz (**h**), and partial voltage (**i**). **j**, φ and C_A at 120 Hz of a single NCEC at different curvatures. Insets are the schematic diagram for the bending deformation of a single NCEC. **k**, Long-term stability test of a single NCEC at curvature of 2 cm^{-1} over 200,000 cycles.